# Femtosecond Quantum Fluid Dynamics of Helium Atom Under an Intense Laser Field

**BIJOY KR. DEY, B. M. DEB***

*Theoretical Chemistry Group, Department of Chemistry, Panjab University, Chandigarh 160014, India*

*Received 10 February 1997; revised 23 April 1998; accepted 8 May 1998*

**ABSTRACT:** A comprehensive, nonperturbative, time-dependent quantum mechanical (TDQM) approach is proposed for studying the dynamics of a helium atom under an intense, ultrashort (femtoseconds) laser pulse. The method combines quantum fluid dynamics (QFD) and density functional theory. It solves a *single* generalized nonlinear Schrödinger equation of motion (EOM), involving time and three space variables, which is obtained from two QFD equations, namely, a continuity equation and an Euler-type equation. A highly accurate finite difference scheme along with a stability analysis is presented for numerically solving the EOM. Starting from the ground-state Hartree–Fock density for He at $t = 0$, the EOM yields the time-dependent (TD) electron density, effective potential surface, difference density, difference effective potential, ground-state probability, $\langle r \rangle$, magnetic susceptibility, polarizability, flux, etc. By a Fourier transformation of the TD dipole moment along the linearly polarized-field direction, the power and rate spectra for photoemission are calculated. Eleven mechanistic routes for photoemission are identified, which include high harmonic generation as well as many other spectral transitions involving ionized, singly excited, doubly excited (autoionizing), and continuum He states, based on the evolution of the system up to a particular time. Intimate connections between photoionization and photoemission are clearly observed through computer visualizations. Apart from being consistent with current experimental

*Correspondence to:* B. M. Deb.

*Also at the Jawaharlal Nehru Centre for Advanced Scientific Research, Bangalore 560064, India.

Contract grant sponsors: Department of Atomic Energy, Bombay, India; Council of Scientific and Industrial Research, New Delhi, India.



CCC 0020-7608 / 98 / 030441-34

and theoretical results, the present results offer certain predictions on spectral transitions which are open to experimental verification.  Int J Quant Chem 70: 441–474, 1998

**Key words:** quantum fluid dynamics; atom–laser interaction; femtosecond dynamics; density functional theory; high harmonic generation

## Introduction

In recent years, the study of atomic behavior under high-intensity laser pulses—which produce electric-field strengths comparable to those produced by atomic nuclei and bombard the atom with a *large* number of photons—has emerged as an important area in both theoretical and experimental research [1–33]. Such phenomena can be studied over a femtosecond time scale. To acquire detailed physical insights into the start-to-finish mechanisms of these processes, time-dependent quantum mechanical (TDQM) formalisms are necessary, which are rigorous, amenable to high-accuracy computation over a large number of time steps, and still possess physical as well as visualizational transparency. It was the purpose of this article to present such a TDQM approach which also admits a ''classical'' interpretation of the events considered, which primarily involve photoionization [18–23, 29] and photoemission [1, 11, 14, 15, 19, 20, 28].

A theoretical treatment of the effects of radiation on an atom may be performed either perturbatively (for ''small'' fields) or nonperturbatively (for ''large'' fields). It is the intensity of incident radiation that decides which of these two approaches should be adopted for studying the atom–radiation interaction. The polarization ($P$) of an atom by an electric field ($E$) may be written as [1]

$$P = \epsilon_0(\chi_1 E + \chi_2 E^2 + \chi_3 E^3 + \cdots), \qquad (1)$$

where $\chi_i$ is the $i$th-order polarizability. The ratio of two successive terms on the right-hand side of Eq. (1) is [1]

$$\frac{\chi_{i+1} E^{i+1}}{\chi_i E^i} \cong \frac{Ed}{\Delta}, \qquad (2)$$

where $d$ is the transition-dipole matrix element and $\Delta$ is the energy detuning of the incident radiation. Substituting typical values for $d(\sim 10^{-29}$ Cm) and $\Delta$ ($\sim 0.5$ eV) indicates that for intensities exceeding $10^{13}$ W cm$^{-2}$ the above ratio surpasses unity and the series in Eq. (1) diverges [1]. Thus, for radiation intensities greater than $10^{13}$ W cm$^{-2}$, a nonperturbative method is required to study the detailed mechanism of the femtosecond dynamics of the atom–radiation interaction.

A direct but rather difficult way to study such dynamics is the temporal and spatial integration of the time-dependent (TD) Schrödinger equation (SE). A compromise route toward this objective is the numerical solution of the SE within the TD Hartree–Fock (HF) approximation where one has to solve a coupled set of $N$ equations for an $N$-electron atom. During the last two decades, the TDHF method has been employed by various workers [1, 5–15] for studying dynamical systems. Burnett et al. [1] discussed the various theoretical approaches employed so far to deal with different aspects of this problem.

Another nonperturbative method of considerable promise comes from TD quantum fluid density functional theory (QF-DFT) [34, 35] which is still in its infancy. This method has recently been formulated and applied to high-energy ion–atom collisions [34, 35] as well as to a limited study [35] of the He atom under an intense laser field. These studies suffered from the limitation that the ionization of the atom was completely excluded and therefore it was not possible to connect the computed results to experimental observations. In this article, we report, for the first time, a realistic comprehensive study of several density-based aspects of the dynamics of a He atom—with particular emphasis on photoemission—under an ultrasharp, high-intensity laser field [36] within the TD-QF-DFT, such that both multiphoton excitation and ionization of the pulsating atom take place, with accompanying photoemission, permitting quite detailed experimental contact.

The quantum fluid dynamical approach [37–42] considers the electron density to be distributed over the whole three-dimensional (3-D) space just like a continuous, ''classical'' fluid. It calculates an

overall, scattered, complex hydrodynamical ''wave function'' $\psi(\mathbf{r}, t)$ by solving a TD generalized nonlinear SE which contains all information on the dynamics of the system under investigation. The conceptual simplicity of this approach rests on its offering a ''classical'' view of quantum systems in terms of local physical observables, namely, the quantum mechanical electronic charge density $\rho(\mathbf{r}, t)$ and current density $\mathbf{j}(\mathbf{r}, t)$ in 3-D space (atomic units employed, unless otherwise specified), where

$$\rho(\mathbf{r}, t) = |\psi(\mathbf{r}, t)|^2, \tag{3}$$

$$\mathbf{j}(\mathbf{r}, t) = [\psi_{re} \nabla\psi_{im} - \psi_{im} \nabla\psi_{re}]. \tag{4}$$

An advantage of this method over other methods, including TDHF theory, is the reduction in the number of equations to only *one* and in the spatial dimensionality from $3N$ to 3. This advantage is partly offset by the disadvantage of having to solve a TD highly nonlinear integrodifferential equation of motion (EOM) for the quantum fluid.

We wish to see whether the present method generates all the physical effects including the mechanism of photoemission in the He-laser dynamics as known at present. With this end in mind, we devised a new, efficient, and accurate numerical scheme for the space–time solution of the EOM. This scheme does not enforce the conservation of the total electronic charge within the computation grid to its initial value at *every* time step and therefore can probe both excitation and ionization of the atom under the external TD perturbation. A stability analysis of our numerical scheme is also presented here. The scheme is quite general and applicable to other TD EOMs, including generalized nonlinear SEs. The present overall approach is also capable of ready extension to atomic systems with more than two electrons and to molecular systems. One simply solves a *single* equation irrespective of the number of electrons in the system. Nevertheless, this single-particle approach does include two-particle effects such as Coulomb, exchange, and correlation and therefore goes beyond the TDHF approximation.

The remainder of this article is as follows: The next section describes the TD-QFD EOM for a He atom under an intense laser field. As mentioned above, this is a single, generalized, nonlinear SE. The third section describes the numerical method and its stability analysis for the spatial and temporal solution of the EOM. The fourth section describes the computed results on photoemission and other features with their visualization and physical interpretation, while the fifth section includes a few concluding remarks.

## A Quantum Fluid Dynamical Treatment of the Interaction of a He Atom with an Ultrasharp, High-intensity Laser Field

### THE TIME-DEPENDENT GENERALIZED NONLINEAR SCHRÖDINGER EQUATION

The current status of TD-DFT [39, 43–45] permits one to write the two basic QFD equations, namely, a continuity equation and an Euler-type EOM, in terms of local observables, the electron density $\rho(\mathbf{r}, t)$, and the current density $\mathbf{j}(\mathbf{r}, t) = \rho \nabla\chi(\mathbf{r}, t)$, where $\chi$ is a velocity potential [34, 35], as

$$\frac{\partial\rho}{\partial t} + \nabla \cdot (\rho \nabla\chi) = 0 \tag{5}$$

$$\frac{\partial\chi}{\partial t} + \frac{1}{2}(\nabla\chi)^2 + \frac{\delta G[\rho]}{\delta\rho} + \int \frac{\rho(\mathbf{r}', t)}{|\mathbf{r} - \mathbf{r}'|} d\mathbf{r}' + v(\mathbf{r}, t) = 0, \tag{6}$$

where $v(\mathbf{r}, t)$ is a TD potential including the electron–nuclear attraction and interaction with the laser field. $G[\rho]$ is a universal DF comprising kinetic and exchange–correlation (XC) energy functionals [46, 47]:

$$G[\rho] = \frac{1}{8}\int \frac{|\nabla\rho|^2}{\rho} d\mathbf{r} + E_{xc}[\rho]. \tag{7}$$

The complex-valued, hydrodynamical ''wave function'' $\psi(\mathbf{r}, t)$ for the entire, time-evolving system is

$$\psi(\mathbf{r}, t) = \rho^{1/2}(\mathbf{r}, t)\exp[i\chi(\mathbf{r}, t)]. \tag{8}$$

Eliminating $\chi(\mathbf{r}, t)$ from Eqs. (5) and (6) yields the following nonlinear SE within a local density approximation:

$$\left[-\frac{1}{2}\nabla^2 + v_{eff}(\rho; \mathbf{r}, t)\right]\psi(\mathbf{r}, t) = i\frac{\partial\psi(\mathbf{r}, t)}{\partial t}, \tag{9}$$

where, taking $E_{xc}$ as $E_x + E_c$, the effective potential $v_{eff}$ is given by ($\rho = |\psi|^2$)

$$v_{eff}(\rho; \mathbf{r}, t) = v_x(\rho) + v_c(\rho) + U(\mathbf{r}, t) + I(\mathbf{r}, t). \tag{10}$$

The terms on the right-hand side of Eq. (10) are exchange, correlation, electrostatic, and interaction potentials, respectively. These are taken as

$$v_x(\rho) = -\frac{4}{3} C_x \rho^{1/3}(\mathbf{r}, t);$$

$$C_x = (3/4\pi)(3\pi^2)^{1/3} \tag{11}$$

$$v_c(\rho) = -\frac{9.810 + 28.583\rho^{-1/3}}{(9.810 + 21.437\rho^{-1/3})^2} \tag{12}$$

$$U(\mathbf{r}, t) = -\frac{Z}{r} + \int \frac{\rho(\mathbf{r}', t)}{|\mathbf{r} - \mathbf{r}'|}\, d\mathbf{r}' \tag{13}$$

$$I(\mathbf{r}, t) = \begin{cases} -\dfrac{1}{|\mathbf{r} - \mathbf{R}(t)|}, \\ \quad \text{for proton–atom collision [34, 35]} & (14) \\ -\boldsymbol{\mu}(\mathbf{r}, t) \cdot \mathbf{E}(t), \\ \quad \text{for interaction with radiation,} & (15) \end{cases}$$

where $Z$ is the nuclear charge of the atom and $\boldsymbol{\mu}(\mathbf{r}, t)$ is the TD (oscillating) dipole moment under the action of the electric field $\mathbf{E}(t)$. In Eq. (10), the combination of Dirac exchange and Wigner-type correlation potentials gives a very good approximation to $v_{xc}$ due to a partial cancellation of errors [48]. The kinetic energy part is dealt with through the Weizsäcker term in Eq. (7); this term gives the exact kinetic energy for a one-electron system and a two-electron Hartree–Fock system. A generalization to systems containing more than two electrons can be made by incorporating an additional ''nonclassical'' density-dependent energy functional $T^{corr}[\rho]$ in Eq. (7), which is the difference between the actual and the Weizsäcker kinetic energy. Although an exact form of $T^{corr}[\rho]$ is unknown, Deb and Ghosh [49] provided a quite accurate prescription for calculating $T^{corr}[\rho]$ numerically (for noble gas atoms), which gives the difference between the HF kinetic energy and the Weizsäcker kinetic energy. Following their work [49], one can rewrite Eq. (7) for many-electron systems, for example, the noble gas atoms, as

$$G[\rho] = \frac{1}{8}\int \frac{|\nabla\rho|^2}{\rho}\, d\mathbf{r} + E_{xc}[\rho] + T^{corr}[\rho] \tag{16}$$

where

$$T^{corr}[\rho] = C_k \int f(\mathbf{r}, t)\, \rho^{5/3}(\mathbf{r}, t)\, d\mathbf{r} \tag{17}$$

and the local system-dependent function $f(\mathbf{r}, t)$ is to be evaluated at each time. Thus, the nonlinear SE for systems with more than two electrons changes into

$$\left[-\frac{1}{2}\nabla^2 + v_{eff}(\rho; \mathbf{r}, t) + \frac{\delta T^{corr}[\rho]}{\delta\rho}\right]\psi(\mathbf{r}, t) = i\frac{\partial\psi(\mathbf{r}, t)}{\partial t}, \tag{18}$$

where

$$\frac{\delta T^{corr}[\rho]}{\delta\rho} = \frac{5}{3} C_k \rho^{2/3}(\mathbf{r}, t)\, g(\mathbf{r}, t) \tag{19}$$

and

$$g(\mathbf{r}, t) = \frac{3}{5} f(\mathbf{r}, t) + \frac{2}{5}\rho^{-2/3}(\mathbf{r}, t) \times \int d\mathbf{r}'\, \rho(\mathbf{r}', t)\, \tilde{\rho}^{-1/3}(\mathbf{r}', t)\frac{\delta\tilde{\rho}(\mathbf{r}')}{\delta\rho(\mathbf{r})} \tag{20}$$

$$f(\mathbf{r}, t) = [\tilde{\rho}(\mathbf{r}, t)/\rho(\mathbf{r}, t)]^{2/3}.$$

Attempts to solve the above equation for many-electron systems where at each time the simultaneous evaluation of $g(\mathbf{r}, t)$, $f(\mathbf{r}, t)$, and $\psi(\mathbf{r}, t)$ is necessary are in progress. A starting, very good approximation is to calculate $f(\mathbf{r}, 0)$ from the HF density. The present work for two-electron systems assumes that $f(\mathbf{r}, t) = g(\mathbf{r}, t) = 0$ [note that the $\tilde{\rho}$ in Eq. (20) has a different meaning compared to the cylindrical coordinate $\tilde{\rho}$ defined later].

Equation (9) describes the complete dynamics of the TD process through the hydrodynamical function $\psi(\mathbf{r}, t)$ and the pulsating effective potential $v_{eff}(\rho; \mathbf{r}, t)$ on which the process occurs. The significance of Eq. (9) was previously discussed by Deb et al. [35]. Since, under the perturbation, many excited/ionized states of the He atom will mix with the ground state, the major assumption made in this work is that the *XC* potential given by Eqs. (11) and (12) is also valid for excited states. This is generally not true. However, this assumption is forced upon us by the current inadequate knowl-

edge about the universal forms of *XC* energy functionals for excited states.

It is worthwhile to note that $\psi(\mathbf{r}, t)$ does not obey a linear superposition principle. However, the highly nonlinear Eq. (9) proceeds much beyond the linear-response approximation since it calculates $\rho(\mathbf{r}, t)$ to all orders of change, which is then employed to calculate the expectation value of the dipole moment.

### LASER SPECIFICATION

For computational convenience, we take a hypothetical laser with the following characteristics:

(i) Electric field,

$$E(t) = E_0 f(t)\sin(\omega_L t);\ E_0 = 0.03995 \text{ au.};\quad \omega_L = 0.13819674 \text{ au } (\lambda_L = 329.7 \text{ nm}); \tag{21}$$

intensity,

$$I = (1/8\pi)cE_0^2 = 5.6 \times 10^{13} \text{ W cm}^{-2} \tag{22}$$

($c$ is the speed of light).

(ii) Temporal pulse-shape function is a Gaussian,

$$f(t) = \begin{cases} e^{-\alpha(t-t_0)^2}, & t < t_0 \\ 1, & t \geq t_0, \end{cases} \tag{23}$$

where $\alpha = 2.59559 \times 10^{-4}$ au and $t_0 = (10\pi)/\omega_L = 227.32755$ au, equivalent to five oscillation periods of the field; each oscillation period is 45.46551 au (1 au of time = 0.0241889 fs). $f(t)$ has a width of $\cong 2.5$ fs, centered at $\cong 5.5$ fs. Such a laser wavelength and pulse function have already been employed by other workers [36, 50] to study the intense-field photodissociation of the $H_2^+$ molecule.

(iii) In cylindrical coordinates $\tilde{\rho}, \tilde{z}, \tilde{\phi}$ ($0 \leq \tilde{\rho} \leq \infty$, $-\infty \leq \tilde{z} \leq +\infty$, $0 \leq \tilde{\phi} \leq 2\pi$), the interaction potential for the He atom in the laser field is taken as

$$I(\mathbf{r}, t) = I(\tilde{z}, t) = -\mu(\tilde{z}, t) E_0 f(t)\sin(\omega_L t), \tag{24}$$

where $\mu(\tilde{z}, t) = \tilde{z}$, taking a linearly polarized laser field.

The computations have been performed for 16.5 oscillation periods ($\cong 18$ fs), assuming that the important features of the TD process would manifest themselves by this time. During the first five periods, the field amplitude increases according to Eq. (23) and then remains constant. The symmetry of the system permits the azimuthal angle $\tilde{\phi}$ to be analytically integrated out so that only the $(\tilde{\rho}, \tilde{z})$ variations need to be studied.

## Numerical Solution of Eq. (9) and Calculation of Miscellaneous Quantities

### THE TIME-PROPAGATOR

Let $\hat{\varphi}$ denote the nonlinear operator within square brackets in Eq. (9) which may then be written as

$$\frac{\partial \psi(\mathbf{r}, t)}{\partial t} = -i\hat{\varphi}(\rho; \mathbf{r}, t)\psi(\mathbf{r}, t) \tag{25}$$

that is,

$$\partial/\partial t = -i\hat{\varphi}. \tag{26}$$

The Taylor expansion of $\psi(\mathbf{r}, t + dt)$ around $\psi(\mathbf{r}, t)$ is given by

$$\begin{aligned} \psi(\mathbf{r}, t + dt) &= \left[1 + dt\frac{\partial}{\partial t} + \frac{1}{2}(dt)^2\frac{\partial^2}{\partial t^2} + \cdots\right]\psi(\mathbf{r}, t) \\ &= e^{dt(\partial/dt)}\psi(\mathbf{r}, t) \\ &= e^{-i\,dt\,\hat{\varphi}}\psi(\mathbf{r}, t), \text{ from Eq. (26).} \end{aligned} \tag{27}$$

Thus, $e^{-i\hat{\varphi}\,dt}$ is the time propagator, which is a nonlinear evolution operator propagating the hydrodynamical "wave function" $\psi(\mathbf{r}, t)$ from $t$ to an advanced time $t + dt$. Therefore, taking $t - t_0$ as small and positive semidefinite, one can write

$$\psi(\mathbf{r}, t) = e^{-i\hat{\varphi}(t-t_0)}\psi(\mathbf{r}, t_0). \tag{28}$$

There are several numerical schemes to evaluate the time propagator [51–53]. One requires a scheme which is both stable and unitary. The method of propagation adopted by us and described below satisfies these requirements, as shown by a stability analysis, and is analogous to Cayley's fractional form of the propagator in one dimension [54].

## THE NUMERICAL SCHEME AND STABILITY ANALYSIS

The He nucleus resides at the center of the cylindrical coordinates $\tilde{\rho}, \tilde{z}, \tilde{\phi}$. After integrating out the azimuthal angle $\tilde{\phi}$, Eq. (9) can be transformed into

$$\frac{\partial \psi}{\partial t} = \left\{ -\frac{1}{2i}\left[\frac{\partial^2}{\partial \tilde{\rho}^2} + \frac{1}{\tilde{\rho}}\frac{\partial}{\partial \tilde{\rho}} + \frac{\partial^2}{\partial \tilde{z}^2}\right] + \frac{v_{eff}(\rho; \tilde{z}, \tilde{\rho}, t)}{i}\right\}\psi. \quad (29)$$

On substituting $\tilde{\rho} = x^2$, Eq. (29) transforms to

$$\frac{\partial \psi}{\partial t} = -\frac{1}{2i}\left[\frac{1}{4x^2}\frac{\partial^2}{\partial x^2} + \frac{1}{4x^3}\frac{\partial}{\partial x} + \frac{\partial^2}{\partial \tilde{z}^2}\right]\psi + \frac{v_{eff}(\rho; \tilde{z}, x, t)}{i}\psi \quad (30)$$

$$= \hat{L}(t, x, \tilde{z}, i, \rho, D_1, D_1^2, D_2^2)\psi, \quad (31)$$

where $\hat{L}$ is a nonlinear operator given by

$$\hat{L} = aD_1^2 + bD_1 + cD_2^2 + \frac{v_{eff}}{i} \quad (32)$$

$$a = -\frac{1}{8x^2 i}$$
$$b = -\frac{1}{8x^3 i}$$
$$c = -\frac{1}{2i}$$
$$D_1 = \frac{\partial}{\partial x} \quad (33)$$
$$D_1^2 = \frac{\partial^2}{\partial x^2}$$
$$D_2^2 = \frac{\partial^2}{\partial \tilde{z}^2}.$$

Analogous to Eq. (27), the equation of propagation for Eq. (29) can be written as

$$\psi(x, \tilde{z}, t + \Delta t) = e^{\Delta t \hat{L}}\psi(x, \tilde{z}, t). \quad (34)$$

Keeping in mind the singularity of the electron–nuclear attractive potential, we discretize $x$, $\tilde{z}$, and $t$ as

$$\begin{aligned} x &= lh \qquad l = 1, 2, \ldots, N_1 \\ \tilde{z} &= mh \qquad m = 1, 2, \ldots, N_2 \\ t &= n\Delta t \qquad n = 1, 2, \ldots, N_3, \end{aligned} \quad (35)$$

where $h$ is the step size for the discretized variables $x$ and $\tilde{z}$.

In this discretized grid, Eq. (34) can be written in a local form as

$$\psi_{l,m}^{n+1} = e^{\Delta t \hat{L}}\psi_{l,m}^{n}. \quad (36)$$

This is an explicit scheme, because it involves only one grid point at the advanced time level $t = (n + 1)\Delta t$. For an implicit formula, one can write Eq. (36) in the central form as

$$e^{-(1/2)\Delta t \hat{L}}\psi_{l,m}^{n+1} = e^{(1/2)\Delta t \hat{L}}\psi_{l,m}^{n}. \quad (37)$$

Substituting $\hat{L}$ from Eqs. (32) and (33) into Eq. (37), we obtain

$$e^{-(1/2)\Delta t}\left(aD_1^2 + bD_1 + \frac{v_{eff}}{2i}\right) \times -e^{-(1/2)\Delta t}\left(cD_2^2 + \frac{v_{eff}}{2i}\right)\psi_{l,m}^{n+1} = e^{(1/2)\Delta t}\left(aD_1^2 + bD_1 + \frac{v_{eff}}{2i}\right) \times e^{(1/2)\Delta t}\left(cD_2^2 + \frac{v_{eff}}{2i}\right)\psi_{l,m}^{n}, \quad (38)$$

where the coordinates $x$ and $\tilde{z}$ have been separated.

Since $v_{eff}$ is a scalar, an operation by its exponential on the ''wave function'' $\psi$ is just multiplying $\psi$ at each grid point by the corresponding exponential. But since $D_1$, $D_1^2$, and $D_2^2$ are the first and second derivatives, operation by their exponentials is not simple multiplication. We used the standard three-point numerical expression for the second derivative of $\psi$ as follows:

$$D_1^2\psi_{l,m}^{n} = \frac{\partial}{\partial x^2}\psi_{l,m}^{n} = \frac{1}{h^2}\delta_x^2\psi_{l,m}^{n} = \frac{1}{h^2}(\psi_{l+1,m}^{n} - 2\psi_{l,m}^{n} + \psi_{l-1,m}^{n}) \quad (39)$$

$$D_2^2\psi_{l,m}^{n} = \frac{1}{h^2}\delta_{\tilde{z}}^2\psi_{l,m}^{n} = \frac{1}{h^2}(\psi_{l,m+1}^{n} - 2\psi_{l,m}^{n} + \psi_{l,m-1}^{n}). \quad (40)$$

For the first derivative, the two-point numerical expression gives

$$D_1\psi_{l,m}^n = \frac{1}{2h}\delta_x\psi_{l,m}^n = \frac{1}{2h}(\psi_{l+1,m}^n - \psi_{l-1,m}^n). \quad (41)$$

The operators $D_1 + D_1^2$ and $D_2^2$ are of tridiagonal matrix from. It is rather difficult to operate with the exponentiated $D_1$, $D_1^2$, or $D_2^2$ operators on the ''wave function'' in position space. In the momentum representation, such operations are much simpler since they would involve diagonal matrices in momentum space. However, we continue with the coordinate representation.

The only way to operate with the exponentiated $D_1$, $D_1^2$, or $D_2^2$ operators on the ''wave function'' in coordinate representation is to truncate the expanded exponential after certain terms, allowing for a permissible error due to truncation. Therefore, on expanding the exponential operators and using Eqs. (39)–(41), Eq. (38) becomes

$$(1 - d\delta_x^2 - e\delta_x - f)\left(1 - g\delta_z^2 - f\right)\psi_{l,m}^{n+1} = (1 + d\delta_x^2 + e\delta_x + f)\left(1 + g\delta_z^2 + f\right)\psi_{l,m}^n, \quad (42)$$

employing truncation after the second term. Since truncation was performed on both sides of the equation, there would be some mutual cancellation of truncation errors. In Eq. (42),

$$d = \frac{a\Delta t}{2h^2}, \quad e = \frac{b\Delta t}{4h}, \quad f = \frac{v\Delta t}{4i}, \quad g = \frac{c\Delta t}{2h^2}. \quad (43)$$

Equation (42) has a local truncation error $0[(\Delta t)^3 + h^2\Delta t]$. The stability analysis of this expression is performed below; it is locally stable under certain conditions which have been incorporated in the present computations.

Now, following the Peaceman–Rachford splitting [55], Eq. (42) leads to the two equations

$$(1 - d_l\delta_x^2 - e_l\delta_x - f_l)\psi_{l,m}^* = \left(1 + g_l\delta_z^2 + f_l\right)\psi_{l,m}^n \quad (44)$$

and

$$\left(1 - g_l\delta_z^2 - f_l\right)\psi_{l,m}^{n+1} = (1 + d_l\delta_x^2 + e_l\delta_x + f_l)\psi_{l,m}^*, \quad (45)$$

where $\psi_{l,m}^*$ is a fictitious solution which bridges $\psi_{l,m}^{n+1}$ with $\psi_{l,m}^n$. The task now left is simply to solve a tridiagonal matrix equation twice, as discussed below.

Equation (44) can be rewritten as a set of $m$ simultaneous equations:

$$\alpha_l y_{l-1,m}^* + \beta_l y_{l,m}^* + \gamma_l y_{l+1,m}^* = h_{l,m}^n, \quad (46)$$

where

$$y_{l,m} = x_l^2\psi_{l,m} \quad (47)$$

$$\alpha_l = (-d_l + e_l)/x_{l-1}^2 \quad (48)$$

$$\beta_l = (1 + 2d_l - f_l)/x_l^2 \quad (49)$$

$$\gamma_l = (-d_l - e_l)/x_{l+1}^2 \quad (50)$$

$$h_{l,m}^n = \frac{(1 + f_l - 2g_l)}{x_l^2}y_{l,m}^n + \frac{g_l}{x_l^2}(y_{l,m+1}^n + y_{l,m-1}^n). \quad (51)$$

Equation (46) can be recast into a tridiagonal matrix equation:

$$\begin{pmatrix} \beta_1 & \gamma_1 & & & \\ \alpha_2 & \beta_2 & \gamma_2 & & \\ \ddots & \ddots & \ddots & \ddots & \\ & \ddots & \ddots & \ddots & \gamma_{N_1-1} \\ & & & \alpha_{N_1} & \beta_{N_1} \end{pmatrix}\begin{pmatrix} y_1^* \\ y_2^* \\ \vdots \\ y_{N_1-1}^* \\ y_{N_1}^* \end{pmatrix} = \begin{pmatrix} h_1^n \\ h_2^n \\ \vdots \\ h_{N_1-1}^n \\ h_{N_1}^n \end{pmatrix}, \quad (52)$$

which can be solved by using a modified Thomas algorithm and the following boundary conditions:

$$\begin{aligned} &y(0, \tilde{z}) = 0 = y(\infty, \tilde{z}), && \forall\ \tilde{z}, t \\ &y(x, \pm\infty) = 0, && \forall\ x, t \\ &y(x, \tilde{z}) \quad \text{known at } t = 0. \end{aligned} \quad (53)$$

The initial input is an HF electron density for the unperturbed (ground-state) He atom [56]. Equation (52) then yields the fictitious solution $\{y^*_{l,m}\}$ which has been employed as the trial input for the solution of Eq. (45). Equation (45) can also be written as a set of $m$ simultaneous equations:

$$\alpha_l y^{n+1}_{l,m-1} + \beta_l y^{n+1}_{l,m} + \gamma_l y^{n+1}_{l,m+1} = h^n_{l,m}, \quad (54)$$

where

$$\alpha_l = -\frac{g_l}{x_l^2} \quad (55)$$

$$\beta_l = (1 + 2g_l - f_l)/x_l^2 \quad (56)$$

$$\gamma_l = -\frac{g_l}{x_l^2} \quad (57)$$

$$h_{l,m} = \left[(1 - 2d_l + f_l)/x_l^2\right] y^*_{l,m} + \frac{(d_l + e_l)}{x^2_{l+1}} y^*_{l+1,m} + \frac{(d_l - e_l)}{x^2_{l-1}} y^*_{l-1,m}. \quad (58)$$

For a given $l$, Eq. (54) has the tridiagonal form

$$\begin{pmatrix} \beta_1 & \gamma_1 & & & \\ \alpha_2 & \beta_2 & \gamma_2 & & \\ \ddots & \ddots & \ddots & \ddots & \\ & \ddots & \ddots & \ddots & \gamma_{N_2-1} \\ & & \alpha_{N_2} & & \beta_{N_2} \end{pmatrix} \begin{pmatrix} y_1^{n+1} \\ y_2^{n+1} \\ \vdots \\ y_{N_2-1}^{n+1} \\ y_{N_2}^{n+1} \end{pmatrix} = \begin{pmatrix} h_1 \\ h_2 \\ \vdots \\ h_{N_2-1} \\ h_{N_2} \end{pmatrix}. \quad (59)$$

As before, by employing a modified Thomas algorithm, the boundary conditions (53), and $\{y^*_{l,m}\}$ as the trial input, we obtain $\{y^{n+1}_{l,m}\}$. Repeating the same method $N_3$ times will successively yield $\{y^1_{l,m}\}, \{y^2_{l,m}\}, \ldots, \{y^{N_3}_{l,m}\}$.

We now report the *stability analysis* of the above algorithm according to the Von Neumann method for constant coefficients [55, 57], assuming that the method can be applied locally with variable coefficients. There is much numerical evidence [55] to support this. Accordingly, we transform the difference equation into the corresponding error equation [55], which in the present case is of the form

$$(1 - d\delta_x^2 - e\delta_x - f)\left(1 - g\delta_z^2 - f\right)\zeta^{n+1}_{l,m} + 0\{(\Delta t)^3 + h^2\Delta t\} = (1 + d\delta_x^2 + e\delta_x + f)\left(1 + g\delta_z^2 + f\right)\zeta^n_{l,m} + 0\{(\Delta t)^3 + h^2\Delta t\}, \quad (60)$$

where $\zeta_{l,m}$ is the difference between the theoretical $y_{l,m}$ and the numerical $y_{l,m}$ solutions of the difference equation to be solved. Now, a harmonic decomposition is made of the form

$$\zeta^n_{l,m} = e^{\alpha nk} e^{i\beta lh} e^{i\gamma mh}. \quad (61)$$

The error will not grow beyond $e^{i\beta lh}e^{i\gamma mh}$ with time if the growth factor $e^{\alpha k}$ is such that $|e^{\alpha k}| \le 1$ for all $\alpha$. Now, substituting $\zeta^n_{l,m}$ into Eq. (60), we obtain the growth factor as

$$e^{\alpha k} = \frac{(1 + d\delta_x^2 + e\delta_x + f)e^{i\beta lh}\left(1 + g\delta_z^2 + f\right)e^{i\gamma mh}}{(1 - d\delta_x^2 - e\delta_x - f)e^{i\beta lh}\left(1 - g\delta_z^2 - f\right)e^{i\gamma mh}}. \quad (62)$$

By operating with $\delta_x$, $\delta_x^2$, and $\delta_z^2$ on the corresponding exponential function and simplifying, the growth factor is converted to

$$e^{\alpha k} = \frac{(1 - 4d\sin^2(\beta h/2) - 2ie\sin(\beta h) + f)(1 - 4g\sin^2(\gamma h/2) + f)}{(1 + 4d\sin^2(\beta h/2) + 2ie\sin(\beta h) - f)(1 + 4g\sin^2(\gamma h/2) - f)}. \quad (63)$$

Applying the stability condition $|e^{\alpha k}| \le 1$ and then simplifying, we obtain

$$\frac{2\Delta t ib}{h}\sin(\beta h) + 2\frac{(\Delta t)^2 iav_{eff}}{h^2}\sin^2(\beta h/2) \ge 1. \quad (64)$$

Now, substituting the values of $a$, $b$, and $c$ from Eq. (33) into Eq. (64) leads to the stability condition

$$\frac{3\Delta t}{4l^3h^4}\sin(\beta h) - \frac{(\Delta t)^2 v_{eff}}{4l^2h^4}\sin^2(\beta h/2) + \frac{(\Delta t)^2}{8l^6h^8}\sin^2(\beta h/2) \ge 1. \quad (65)$$

It is thus observed that both $\Delta t$ and $h$ are grid-dependent (i.e., $l$-dependent) as well as interdependent. Hence, both are equally important for maintaining stability. Condition (65) was incorporated into our calculations.

The Coulomb repulsion potential in cylindrical coordinates, $Q(\tilde{\rho}, \tilde{z}, \tilde{\phi})$, is calculated by considering $|\mathbf{r} - \mathbf{r}'|^{-1}$ as the Green function of the Laplacian operator [58]. Taking

$$Q(\tilde{\rho}, \tilde{z}, \tilde{\phi}) = \int \frac{\rho(\mathbf{r}')}{|\mathbf{r} - \mathbf{r}'|}\, d\mathbf{r}' \tag{66}$$

and integrating with respect to $\tilde{\phi}$ leads to the expression

$$Q(\tilde{\rho}, \tilde{z}) = 4\pi^2 \int_0^{\infty} \int_{-\infty}^{+\infty} \int_0^{\infty} \rho(\tilde{\rho}', \tilde{z}') J_0(k\tilde{\rho}) J_0(k\tilde{\rho}') \times e^{-k|\tilde{z} - \tilde{z}'|} \tilde{\rho}'\, d\tilde{\rho}'\, d\tilde{z}'\, dk, \tag{67}$$

where $J_0$ is the spherical Bessel function. The integration with respect to $k$ was performed by the Gauss–Legendre quadrature, while that with respect to $\tilde{\rho}'$ and $\tilde{z}'$ was by the trapezoidal method.

The computation grid for the present calculations is defined as follows: After a number of trial runs,

$$0.03 \le x \le 2.25;\ -3.3 \le \tilde{z} \le 3.3;\ 0 \le t \le \frac{2971\pi}{90\omega_L};$$

$$\Delta x = \Delta \tilde{z} = 0.03;$$

$$\Delta t = \begin{cases} \dfrac{\pi}{2700\omega_L}, & \text{up to the 30th time step} \\ \dfrac{\pi}{90\omega_L}, & \text{after the 30th time step} \end{cases}$$

where $\pi/\omega_L = 22.732755$ au. $N_1$ is the total number of grid points in $x = 75$, $N_2$, total number of grid points in $\tilde{z} = 221$, and $N_3$, total number of grid points in $t = 3000$.

As mentioned before, the density at $t = 0$ is the HF density of He atom in the ground state [56]. The HF density is consistent with the hydrodynamical equation [Eq. (25)] for the following reasons: We recently showed [53] that if one follows an imaginary-time evolution of the electron density according to Eq. (25) one obtains the static electron density, corresponding to $t = 0$, based on the search for a global minimum of the expectation value of $\hat{\varphi}$. For the He atom, we calculated the overlap between the resultant static hydrodynamical wave function (normalized to unity) and the HF wave function as 0.99439. A similar imaginary-time evolution of the electron density for the Ne atom gives the ground-state density (with shell structure) and ground-state energy as $-128.8734$ au [53] compared to the exact nonrelativistic value of $-128.939$ au.

In performing TDHF calculations, it was observed by other workers [5, 59, 60] that, even close to the beginning ($t$ close to zero) of the interaction, the electron density spreads all over the space grid including the grid periphery where, initially ($t = 0$), the electron density was taken to be zero. To deal with this problem, one may either add an absorbing potential [5, 59, 60] for the grid periphery or employ a very large grid. The former generally destroys all information about the electron density beyond the defined grid size while the latter is computationally prohibitive. However, the present computations do not suffer from this problem and so we have not adopted either of the above two approaches. In our calculations, significant electron density moves near the grid periphery only around the 550th time step, that is, $t \simeq 131.5$ au ($\sim 3.2$ fs). We feel that this is an actual physical effect (ionization) of the TD perturbation which manifests itself more vividly as the interaction progresses. Note that the boundary conditions (53) put the electron density to zero at the grid periphery for all time. Since the numerical scheme discretizes a continuum grid, the convergence of the approximate to the actual results in the continuum grid will be guaranteed only if both $\Delta\tilde{z}, \Delta x \to 0$. However, note that a convergent solution is not necessarily stable, whereas the reverse is always true provided both $\Delta\tilde{z}$ and $\Delta x$ are sufficiently small [61]. Our numerical scheme satisfies the stability condition [58, 62]

$$\|U\| = \sqrt{\langle |e^{-i\Delta t H}\psi|^2 \rangle} = \sqrt{\langle |\psi(t + \Delta t)|^2 \rangle} \le 1, \tag{68}$$

where $\psi$ is the hydrodynamical ''wave function'' normalized to unity at $t = 0$.

This is not only necessary and sufficient for stability but it also guarantees that errors due to the discretized approximation scheme itself and rounding errors always present in floating point computations cannot grow indefinitely. Accordingly, we selected an optimal grid size which yields a total electronic charge of 1.99939, instead of exactly 2, at the beginning ($t = 0$) of the interaction.

This sacrifice of 0.03% in the total number of electrons may be considered acceptable. The choice of the optimal grid $(N_1, N_2)$ is based on the fact that changes in $N_1$ and $N_2$ do not lead to any significant change in the total electronic charge. Thus, the grid has the capacity to contain all the electrons within it, if no ionization takes place. Our numerical scheme has a local error, $\Delta\xi^{loc} = 0[\Delta t^3 + h^2\Delta t]$ [see Eq. (60)], which appears on both sides of Eq. (42). Obviously, there would be a mutual cancellation of errors and the actual error, $\Delta\xi^{ac}$, will be such that $\Delta\xi^{ac} \leq \Delta\xi^{loc}$. In other words, the maximum error in our calculation due to the discretized space–time grid is $\Delta\xi^{max} = 0[\Delta t^3 + h^2\Delta t]$. Based on this, we give below the expressions relating actual value (*ac*), calculated value (*cal*), and maximum errors (*max*) of different time-dependent properties:

$$\rho_{l,m}^{ac} = \rho_{l,m}^{cal} \pm (\Delta\xi^{max})^2 \pm 2\Delta\xi_{l,m}^{max}\rho_{l,m}^{cal^{1/2}} \quad (69)$$

$$N^{cal} = N^{ac} + N_1N_2(\Delta\xi^{max})^2h^2 + 2\Delta\xi^{max}h^2 \quad (70)$$

$$\langle A\rangle^{cal} = \langle A\rangle^{ac} + h^2(\Delta\xi^{max})^2\sum_{l,m} A_{l,m}\rho_{l,m}^{cal} + 2h^2\Delta\xi^{max}\sum_{l,m} A_{l,m}\rho_{l,m}^{cal^{1/2}}. \quad (71)$$

$\rho_{l,m}$ in Eqs. (69) and (71) is the electronic density at the $(l, m)$ grid point; $N$, the total electronic charge; $A$, an operator; and $A_{l,m}$, the operator at $(l, m)$ grid point. Thus, an estimate of the maximum errors can be obtained from the above equations. All computations and visualizations were performed in double precision on a workstation.

## VARIOUS TIME-DEPENDENT QUANTITIES

Apart from the incident electric field $E(t)$, the electron density $\rho(\tilde{\rho}, \tilde{z}, t)$ and the effective potential $v_{eff}(\tilde{\rho}, \tilde{z}, t)$, the following TD quantities are considered in this article:

(i) $$\langle\tilde{z}\rangle(t) = \int \tilde{z}\rho(\tilde{\rho}, \tilde{z}, t)\, dV \quad (72)$$

where

$$dV = \tilde{\rho}\, d\tilde{\rho}\, d\tilde{z}\, d\tilde{\phi}. \quad (73)$$

In au, Eq. (72) gives the TD (oscillating) electronic dipole moment in the $\tilde{z}$ direction.

(ii) The diagonal $\tilde{z}$-component of the polarizability tensor is calculated as

$$P_{\tilde{z}\tilde{z}}(t) = \frac{|\langle\tilde{z}\rangle(t)|}{|\langle E(t)\rangle|}, \quad (74)$$

where

$$\langle E(t)\rangle = \int E(t)\rho(\tilde{\rho}, \tilde{z}, t)\, dV. \quad (75)$$

Note that $P_{\tilde{z}\tilde{z}}(t)$ is *not* the dipole polarizability tensor within a linear-response approximation. $P_{\tilde{z}\tilde{z}}(t)$ also incorporates the nonlinear response of the electron density to the laser field $E(t)$.

(iii) $$\langle r\rangle(t) = \int(\tilde{\rho}^2 + \tilde{z}^2)^{1/2}\rho(\tilde{\rho}, \tilde{z}, t)\, dV. \quad (76)$$

(iv) Magnetic susceptibility [62],

$$\chi(t) = -\frac{N_0e^2}{6mc^2}\langle r^2\rangle(t), \quad (77)$$

where $N_0$ is the Avogadro number; $e$, the electronic charge; $m$, the electronic mass; $c$, the speed of light; and

$$\langle r^2\rangle(t) = \int(\tilde{\rho}^2 + \tilde{z}^2)\rho(\tilde{\rho}, \tilde{z}, t)\, dV. \quad (78)$$

$\chi(t)$ also incorporates the nonlinear response.

(v) The total number of electrons at any instant,

$$N(t) = \int \rho(\tilde{\rho}, \tilde{z}, t)\, dV. \quad (79)$$

(vi) The probability of the ground state,

$$P_{gs}(t) = |\langle\psi(0)|\psi(t)\rangle|^2. \quad (80)$$

$1 - P_{gs}(t)$ gives the probability for single- and multiphoton excitation and ionization, since $P_{gs}$ is normalized to unity at $t = 0$.

(vii) Average values of interelectronic Coulomb repulsion and electron–nuclear attraction,

$$\langle V_{ee}\rangle(t) = \frac{1}{2}\int\int \frac{\rho(\mathbf{r}, t)\rho(\mathbf{r}', t)}{|\mathbf{r} - \mathbf{r}'|}\, dV\, dV', \quad (81)$$

$$\langle V_{ne}\rangle(t) = -\int\left(\frac{Z}{r}\right)\rho(\tilde{\rho}, \tilde{z}, t)\, dV, \quad (82)$$

where $\mathbf{r}$ and $\mathbf{r}'$ are points in the $\tilde{\rho}\tilde{z}$ plane.

(viii) Stabilization energy of the electron in the laser electric field,

$$E_{stab}(t) = -\int \rho(\mathbf{r}, t) I(\tilde{z}, t)\, dV, \quad (83)$$

where $I(\tilde{z}, t)$ is given by Eq. (24).

(ix) The dynamical difference density,

$$\Delta\rho(\tilde{\rho}, \tilde{z}, t) = \rho(\tilde{\rho}, \tilde{z}, t) - \rho(\tilde{\rho}, \tilde{z}, \Delta t_2), \quad (84)$$

where, for the sake of internal consistency, we take the initial time as $\Delta t_2$, namely, the second time step, instead of $t = 0$ (this procedure is adopted because the HF density is not an exact solution of Eq. (25), although fairly close to it).

(x) The effective difference potential,

$$\Delta v_{eff}(\rho; \tilde{\rho}, \tilde{z}, t) = v_{eff}(\rho; \tilde{\rho}, \tilde{z}, t) - v_{eff}(\rho; \tilde{\rho}, \tilde{z}, \Delta t_2). \quad (85)$$

(xi) The flux of the electron flow or the divergence of electronic current density, $\nabla \cdot \mathbf{j}$, whose negative is given by $\partial\rho/\partial t$, according to Eq. (5). Since

$$\rho = \psi^*\psi, \quad (3)$$

$$\frac{\partial\rho}{\partial t} = \frac{i}{2}(\psi^* \nabla^2\psi - \psi \nabla^2\psi^*). \quad (86)$$

In the present discretized computation grid, Eq. (86) can be written as

$$\left(\frac{\partial\rho}{\partial t}\right)^n_{l,m} = \frac{i}{2x_l^2 x_{l+1}^2 h^2} \times (y^{*n}_{l,m} y^n_{l+1,m} - y^n_{l,m} y^{*n}_{l+1,m}) + \frac{i}{2x_l^2 x_{l-1}^2 h^2} \times (y^{*n}_{l,m} y^n_{l-1,m} - y^n_{l,m} y^{*n}_{l-1,m}) \quad (87)$$

where $y^{*n}_{l,m}$ is the complex conjugate of $y^n_{l,m} = \tilde{\rho}\psi^n_{l,m}$.

## PHOTOEMISSION

As a result of multiphoton interaction with the laser field, the time-evolved density becomes a complicated mixture of densities from a large number of doubly excited (autoionizing), singly excited, continuum states and ''dressed'' states of the He atom as well as states of $He^+$. Such a mixture of densities has been largely unscrambled except for ''dressed'' states which have not been identified; however, many states have been identified by calculating the energy spectral density, ESD($\omega$), that is, the probability per unit volume for a state of energy $\hbar\omega$, $-\infty \le \omega \le +\infty$, through a fast Fourier transformation (FFT) of the time variable of the complex autocorrelation function, $\langle\psi(0)\,|\,\psi(t)\rangle$ [63]. These states enable us to explain much of the detailed dynamics of both photoionization [64] and photoemission (present article) which are preceded mainly by multiphoton excitation from the ground state of He into the above states.

Thus, one may envisage the following main mechanistic routes for photoemission (except transitions between ''dressed'' states, which have not been identified), each route involving many excited/ionized states (g.s., * and ** denote ground, singly excited, and doubly excited state, respectively):

Route a: He* → He(g.s.)
Route b: He*(higher) → He*(lower)
Route c: He** → He(g.s.)
Route d: He**(higher) → He**(lower)
Route e: He** → He*
Route f: $He^+$* → $He^+$(g.s.)
Route g: $He^+$*(higher) → $He^+$*(lower)
Route h: Continuum → He(g.s.)
Route i: Continuum → He**
Route j: Continuum → He*
Route k: Continuum(higher) → continuum (lower)

Because of the autoionizing nature of the He** states, the transitions corresponding to routes *c* and *e* should have lower probability than has route *d*. Routes *h*–*k* are associated with high-harmonic (HH) generation $n\omega_L$, where $3 \le n(\text{odd}) \le 21$. The quantum mechanical HH cutoff rule is given by [15]

$$n_{max} = \left[3.17U_p + U_I F(U_I/U_P)\right]/\omega_L, \quad (88)$$

where $U_I$ is the ionization potential of the atom, $U_P$ is the ponderomotive potential (mean kinetic energy acquired by a free electron in the oscillating

laser field of a given strength), and the factor $F(U_I/U_P)$ is 1.3 for $U_I \ll U_P$, approaching unity as the ratio $U_I/U_P$ increases. In the present calculations, $U_I = 2.90372$ au [68] and $U_P = 0.02087$ au, so that

$$n_{max} = 21.$$

Note that since the Keldysh parameter [29]

$$\gamma = (U_I/2U_P)^{1/2} = 8.34, \text{ i.e., } \gamma > 1, \quad (89)$$

the present atom–laser interaction is in the multiphoton regime. Thus, photoemission by He atom under the intense laser field includes not only HH generation, but also other multiphoton and single-photon transitions given by routes a–g above. Some of these can overlap on the appropriate $n\omega_L$ transitions.

The relative importance of the individual routes a–k can be deduced by calculating the power spectrum and rate spectrum for photoemission. The power spectral density, PSD($\omega$), is obtained through a fast Fourier transform (FFT) of the oscillating dipole moment, $\mu^{\tilde{z}}(t) = \langle \tilde{z} \rangle(t)$, given by Eq. (72), as follows:

We first argue that $\mu^{\tilde{z}}(t)$ is an ensemble of various state-to-state transition moment integrals (TMI). For this, we approximate the TD hydrodynamical ''wave function'' as

$$\psi(\tilde{\rho}, \tilde{z}, t) = \sum_n a_n(t)\phi_n(\tilde{\rho}, \tilde{z})e_n^{-i\omega t}, \quad (90)$$

where $\phi_n$ corresponds to the $n$th energy level which may be degenerate. This enables us to write

$$\mu^{\tilde{z}}(t) = \int \psi^*(\tilde{\rho}, \tilde{z}, t)\tilde{z}\psi(\tilde{\rho}, \tilde{z}, t)\, dV \quad (91)$$

$$= \sum_{n,m} a_n^*(t)a_m(t)e_{nm}^{i\omega t}d_{nm}^{\tilde{z}}, \quad (92)$$

where

$$d_{nm}^{\tilde{z}} = \int \phi_n^*(\tilde{\rho}, \tilde{z})\tilde{z}\phi_m(\tilde{\rho}, \tilde{z})\, dV \quad (93)$$

is the TMI for the transition $\phi_n \leftarrow \phi_m$ and $\omega_{nm} = |\omega_n - \omega_m|$. Thus, $\mu^{\tilde{z}}(t)$ contains information about all possible transitions. The Fourier transform of $\mu^{\tilde{z}}(t)$ is given by

$$d(\omega) = \int \mu^{\tilde{z}}(t)e^{i\omega t}\, dt, \qquad -\infty \le \omega \le +\infty \quad (94)$$

$$= \sum_{n,m} d_{nm}^{\tilde{z}} \int a_n^*(t)a_m(t)e^{i(\omega-\omega_{nm})t}\, dt \quad (95)$$

$$= \sum_{n,m} d_{nm}^{\tilde{z}} A_{nm}(\omega)\delta(\omega - \omega_{nm}). \quad (96)$$

Equation (96) implies that, due to the presence of the $\delta$ function, $\mu^{\tilde{z}}(t)$ can be resolved into various state-to-state transition moments corresponding to transition frequencies $\omega_{nm}$. This resolution is most pronounced if the infinite time record of $\mu^{\tilde{z}}(t)$ is available.

The PSD($\omega$) and the rate spectral density, RSD($\omega$), are given by ($c$ is the velocity of light)

$$\text{PSD}(\omega) = \frac{1}{6\hbar}\left(\frac{4\pi}{c}\right)^3 |d(\omega)|^2 \quad (97)$$

$$\text{RSD}(\omega) = \omega^3 \text{PSD}(\omega). \quad (98)$$

PSD($\omega$) gives the photoemission power per unit time per unit volume corresponding to the frequency $\omega$, while RSD($\omega$) gives the rate of photoemission per unit volume for the same frequency.

To compute the FFT, the integral in Eq. (94) is approximated by a discrete sum over the sampled values of $\mu^{\tilde{z}}(t)$, that is,

$$d(\omega_n) = \int_{-\infty}^{+\infty} \mu^{\tilde{z}}(t)e_n^{i2\pi ft}\, dt$$

$$= \sum_{l=0}^{N-1} \mu_l^{\tilde{z}} e_n^{i2\pi ft} l\Delta t$$

$$= \Delta t \sum_{l=0}^{N-1} \mu_l^{\tilde{z}} e^{i2\pi ln/N}. \quad (99)$$

The FFT transforms the time-grid $t_l = l\Delta t$, where $l = 0, 1, 2, \ldots, N$, to its conjugate $f$ grid, with grid points $f_n = -(1 - n + N/2)/(N\Delta t)$ for $2 \le n \le (N/2) - 1$. The grid value of $f$ at $n = N/2$, namely, the Nyqvist frequency, is given by $f_n = 1/(2\Delta t)$. The FFT algorithm requires that $N$, the total number of sampled values, must be an integer power of 2. For the present computations, $N = 2^{11} = 2048$ ($t = 517.29647$ au $= 12.512833$ fs), although we have allowed the density to evolve up to 3000 time steps [$t = (2971/90)(\pi/\omega_L) = 750.4335$ au $= 18.15216$ fs]. Since we wish to deal with photoemission, PSD($\omega$) is expressed as

$$\text{PSD}(\omega) = \frac{1}{6\hbar}\left(\frac{4\pi}{c}\right)^3 \{|d(\omega)|^2 + |d(-\omega)|^2\}, \quad 0 \le \omega \le \infty. \quad (100)$$

Since $\mu^{\bar{z}}(t)$ is real, $d(\omega) = d(-\omega)$ and, therefore,

$$\mathrm{PSD}(\omega) = \frac{1}{3\hbar}\left(\frac{4\pi}{c}\right)^3 |d(\omega)|^2, \qquad 0 \le \omega \le \infty. \tag{101}$$

For a particular frequency $\omega_n$, the percent contributions to the total power spectral density (TPSD) and to the total rate spectral density (TRSD) are given, respectively, by

$$\frac{\mathrm{PSD}(\omega_n)}{\mathrm{TPSD}} \times 100 \qquad \text{and} \qquad \frac{\mathrm{RSD}(\omega_n)}{\mathrm{TRSD}} \times 100, \tag{102}$$

where, using the triangle approximation,

$$\mathrm{TPSD} = \frac{1}{2}\sum_n \mathrm{PSD}(\omega_n)\, d\omega_n \tag{103}$$

$$\mathrm{TRSD} = \frac{1}{2}\sum_n \mathrm{RSD}(\omega_n)\, d\omega_n, \tag{104}$$

$d\omega_n$ being the width of the resonance at $\omega_n$. Similarly, the photoemission cross-section (PEC) for a given frequency is calculated as

$$\mathrm{Sc}(\omega) = \frac{\mathrm{RSD}(\omega)}{\mathrm{PSD}(\omega)} \times (1/2)\, d\omega, \tag{105}$$

where $d\omega$ is the peak base width in $\omega$. The total PEC is calculated by dividing the total integrated area under all the rate spectral lines by the total integrated area under all the power spectral lines.

## Results and Discussion

Figure 1 displays both the oscillating laser electric field, $E(t)$, and the total number of electrons, $N(t)$. Because of the Gaussian pulse-shape function [Eq. (23)], $E(t)$ begins to build up significantly at $t \cong 130$ au. Figure 2 shows much faster, nonlinear oscillations of both the interelectronic repul-

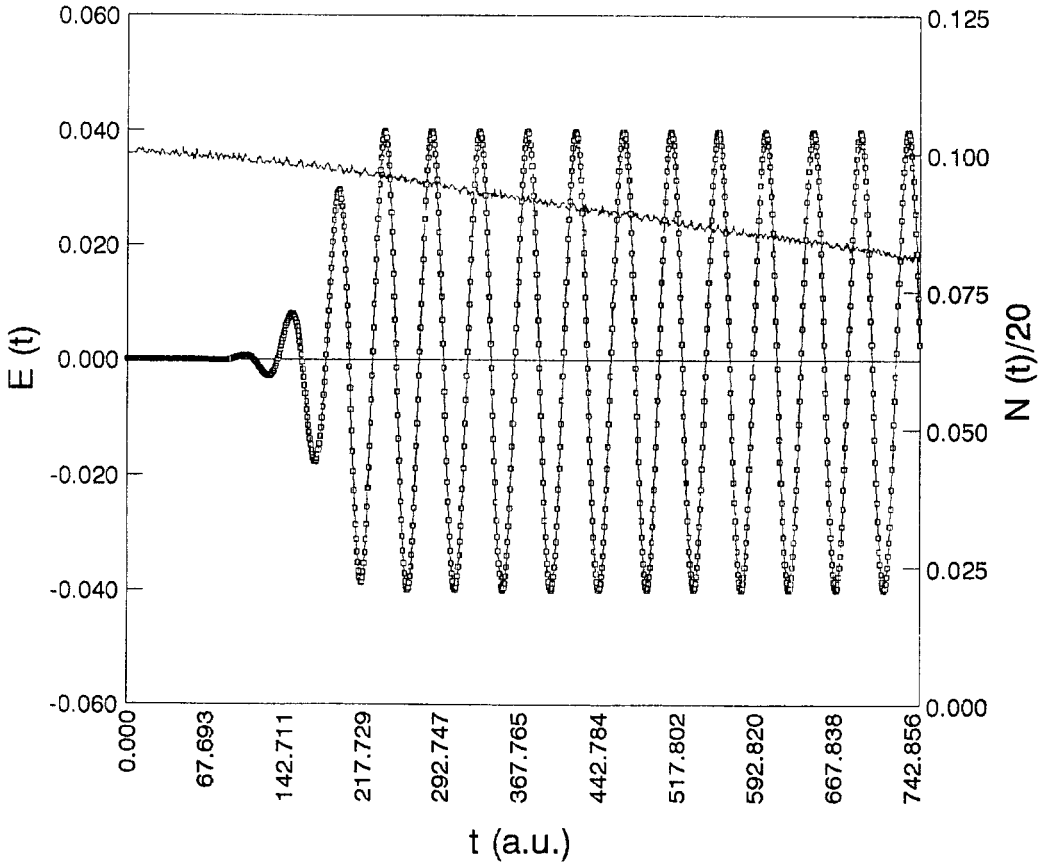


**FIGURE 1.** Plot of periodically oscillating laser electric field, $E(t)$, and total number of electrons, $N(t)$, against time, in au. The ordinate on the left-hand side represents $E(t)$, whereas that on the right-hand side represents $N(t)/20$.

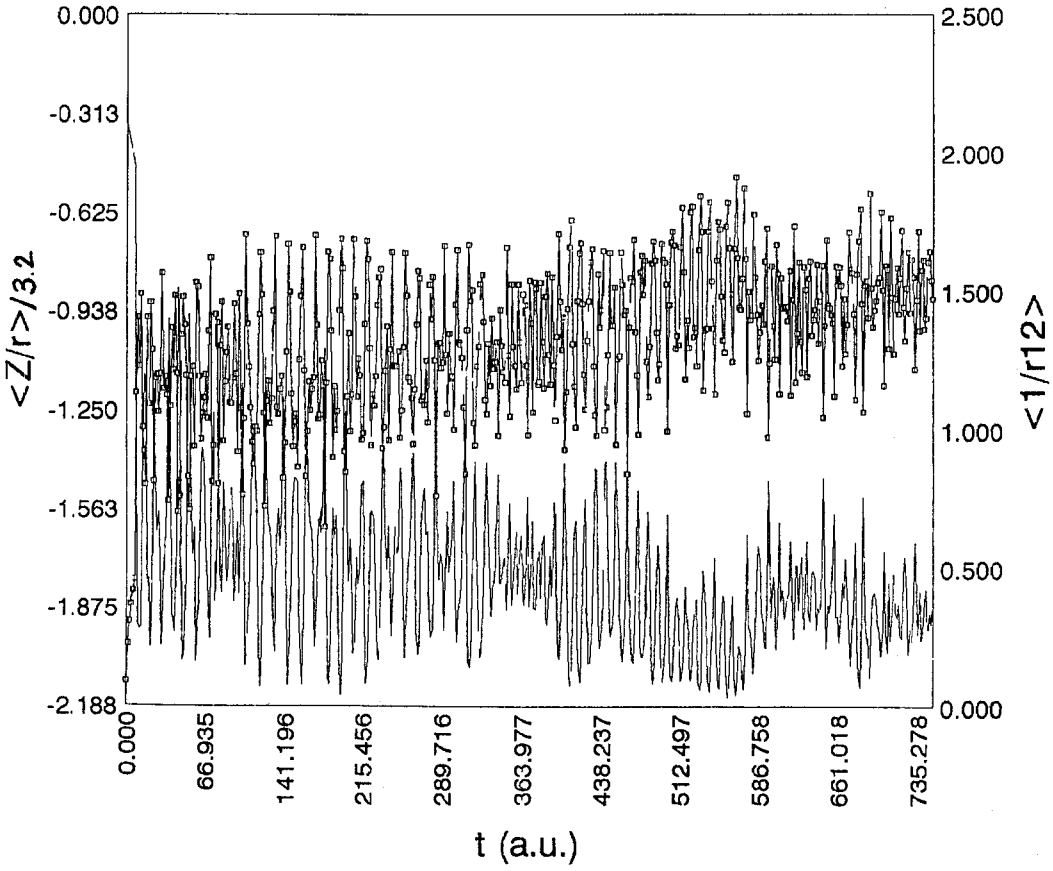


**FIGURE 2.** TD nonlinearly oscillating $\langle Z/r \rangle$ and $\langle 1/r_{12} \rangle$ plotted against time in au. The ordinate on the left-hand side represents $\langle Z/r \rangle / 3.2$, whereas that on the right-hand side represents $\langle 1/r_{12} \rangle$.

sion, $\langle 1/r_{12} \rangle(t)$, and the electron–nuclear attraction, $-\langle Z/r \rangle(t)$. Clearly, $\langle 1/r_{12} \rangle(t)$ represents the overall dynamical interaction (Coulomb, exchange, and correlation) between the two electrons, averaged over all states present in the complicated mixture of state densities, $\rho(\mathbf{r}, t)$. The decrease in $\langle 1/r_{12} \rangle$ with time is faster than that in $-\langle Z/r \rangle$, for example, at $t = 417.2723$, the values of $\langle 1/r_{12} \rangle$ and $\langle Z/r \rangle$ become $\cong 32\%$ and $\cong 55\%$, respectively, of their initial ($t = 0$) values, whereas at $t = 750.4335$, these values are $\cong 8\%$ and $\cong 38\%$, respectively, of their initial values. This is in favor of the fact that electrons move away from each other faster than from the nucleus; this also implies that in spite of progressive ionization a part of the electron density keeps returning to regions close to the nucleus. The change in the total electronic charge, $N(t)$, is a combined effect of changes in both $-\langle Z/r \rangle$ and $\langle 1/r_{12} \rangle$. A faster fall of $\langle 1/r_{12} \rangle$ also implies that under the laser field the atom is now governed mainly by an independent-particle model. Thus, the dynamics are controlled by the helium nucleus which has been found to retain its domination by 38% even at $t = 750.4335$. However, the extra stabilization energy, $E_{stab}(t)$ (see Fig. 3), provided to the electrons by the laser field, is rather low compared to the Coulomb energy of attraction. Thus, instead of providing any extra stability to the electrons, the laser photons become absorbed by the atom for excitation to different excited states (including the continuum) of the He atom, namely, singly and doubly excited states, Floquet ''dressed'' states, Rydberg states, and Stark-shifted states.

A higher absorption of laser photons by the atom can be attributed to increased domination of the nuclear Coulomb field (by its higher value of $\langle Z/r \rangle$) over the laser electric field (by its lower

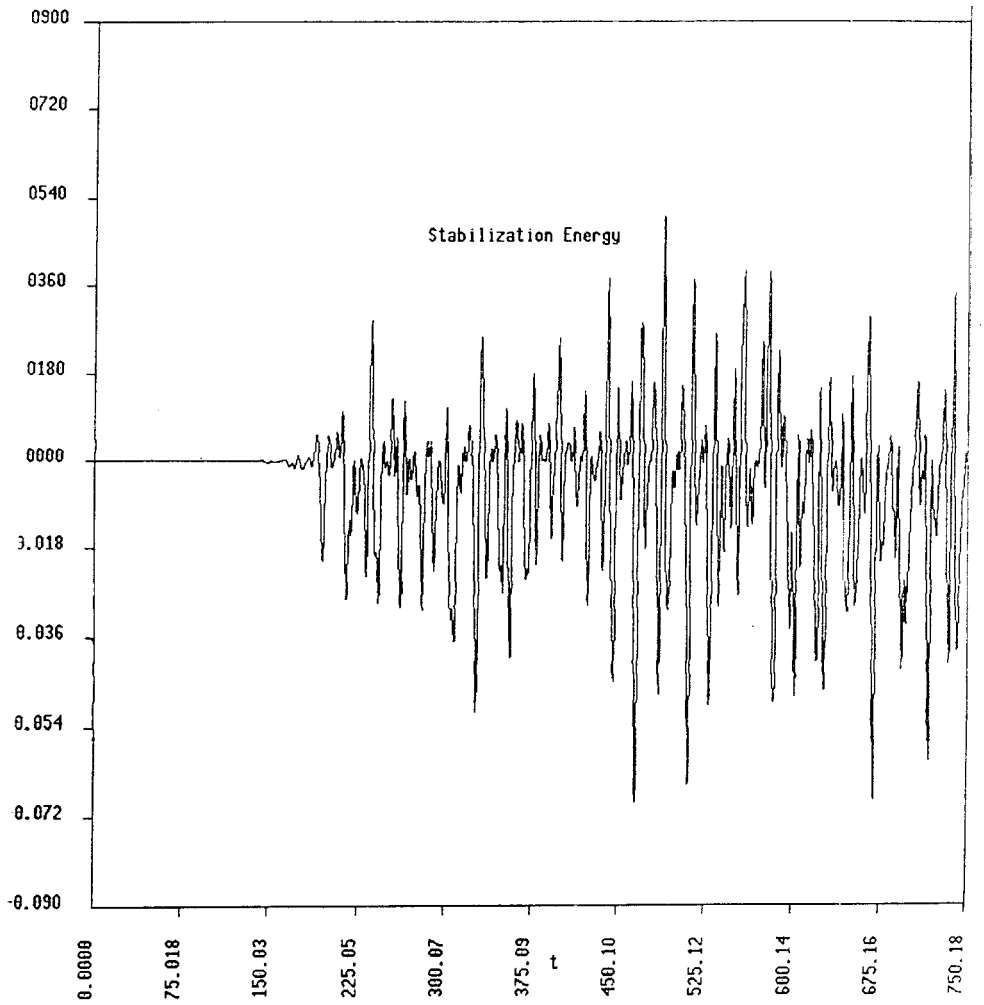


**FIGURE 3.** TD stabilization energy $E_{stab}(t)$ plotted against time, in au.

value of $E_{stab}$) in controlling the dynamics of electrons. This is in sharp contrast to the superintense laser field which dominates over the nuclear field, such that instead of ionization taking place suppression of ionization occurs. Our recent calculations [65] for $I = 5.6 \times 10^{18}$ W cm$^{-2}$, using the present methodology, reveal the mechanism of suppression of ionization; here, $E_{stab}$ can exceed the electron–nuclear attraction energy. It may also be noted that a lowering of electron–nuclear attraction can lead to the excitation of electrons above the first ionization threshold (FIT) or the second ionization threshold (SIT) through many intermediate singly or doubly excited states and consequent ionization. The progress of ionization is indicated by the decrease of $N(t)$ with time (see Fig. 1). So far, the standard technique for reducing the norm of the wave function in the course of interaction is to put an absorbing optical potential at a suitable position depending on the response of the system to the external field. However, our experience has been that incorporation of such an optical potential could make the numerical solution intractable because the Hamiltonian becomes non-Hermitian; also, the choice of the form and a suitable position for such a potential are difficult to decide. In other words, if an absorbing potential is incorporated, then the propagator $e^{-iH't}$ is no longer unitary since $H'$ is non-Hermitian. However, in our method, the propagator is always unitary. Thus, the norm of the hydrodynamical wave function will always remain fixed unless

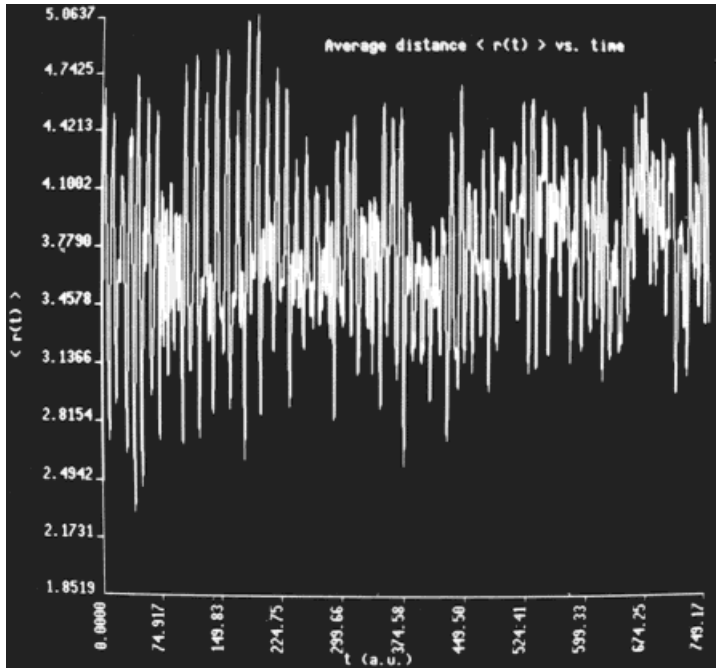


**FIGURE 4.** TD, nonlinearly oscillating $\langle r \rangle(t)$ plotted against time, in au. The oscillation amplitude first increases and then decreases due to progress in photoionization.

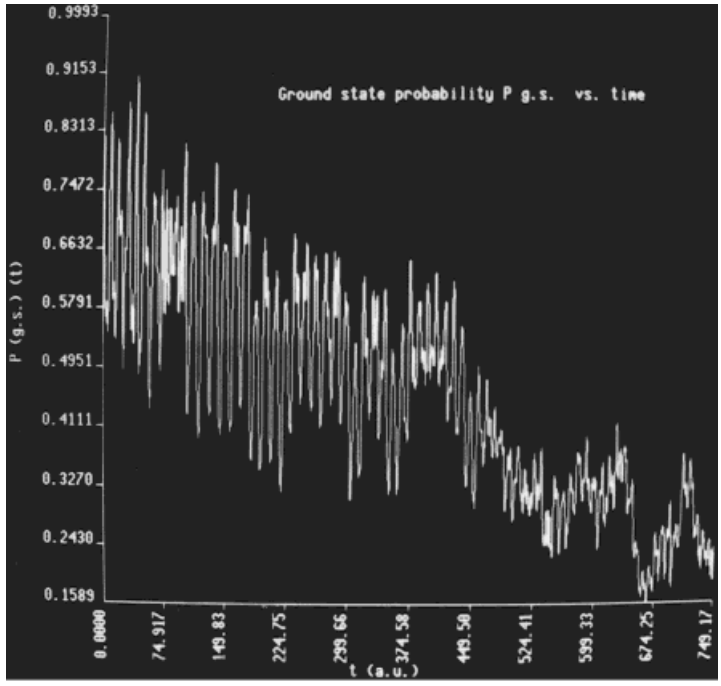


(a)

**FIGURE 5.** Plot of rapidly oscillating ground-state probability, $P_{\text{g.s.}}(t)$ against time, in au: (a) plot for the whole time range; (b) plot for the first 30 time steps, $\Delta t = \pi / 2700\,\omega_L$; (c) plot for the next 25 time steps, $\Delta t = \pi / 90\,\omega_L$. A slow monotonic decrease in $P_{\text{g.s.}}$ is noticed up to the 43rd time step.

there is some withdrawal mechanism (ionization) from any region of the computation grid. The reason for declining $N(t)$ in the present method is because of its setting the density to vanish whenever it reaches to the periphery of the 2-D box, assuming that at the periphery electrons feel negligible attraction due to the nucleus placed at the centre of the box.

Figure 4 shows $\langle r \rangle(t)$ oscillating nonlinearly in an apparently chaotic manner so that the amplitude first increases and then gradually decreases with progress in ionization; a similar pattern is observed with $\mu^{z}(t)$. Figure 5(a) shows the oscillating, gradually decreasing ground-state probability from which it can be inferred that excitation is quite faster than ionization and, therefore, the former precedes the latter. Note that the validity of Eq. (80) demands that there is no abrupt fall in the ground-state probability when the laser field is being switched on. This is seen more clearly in Figure 5(b) and (c), which shows a slow and monotonic decrease in $P_{\text{g.s.}}(t)$ up to the 43rd time step. Thus, at $t \cong 131.6$ au, the ground-state probability has decreased by 57%, whereas $N(t)$ has decreased by only 0.7% ; at $t = 750.4335$ au, these values are 74 and 18%, respectively. The laser field and its interaction with matter are known to differ from other radiations in the sense that they deliver

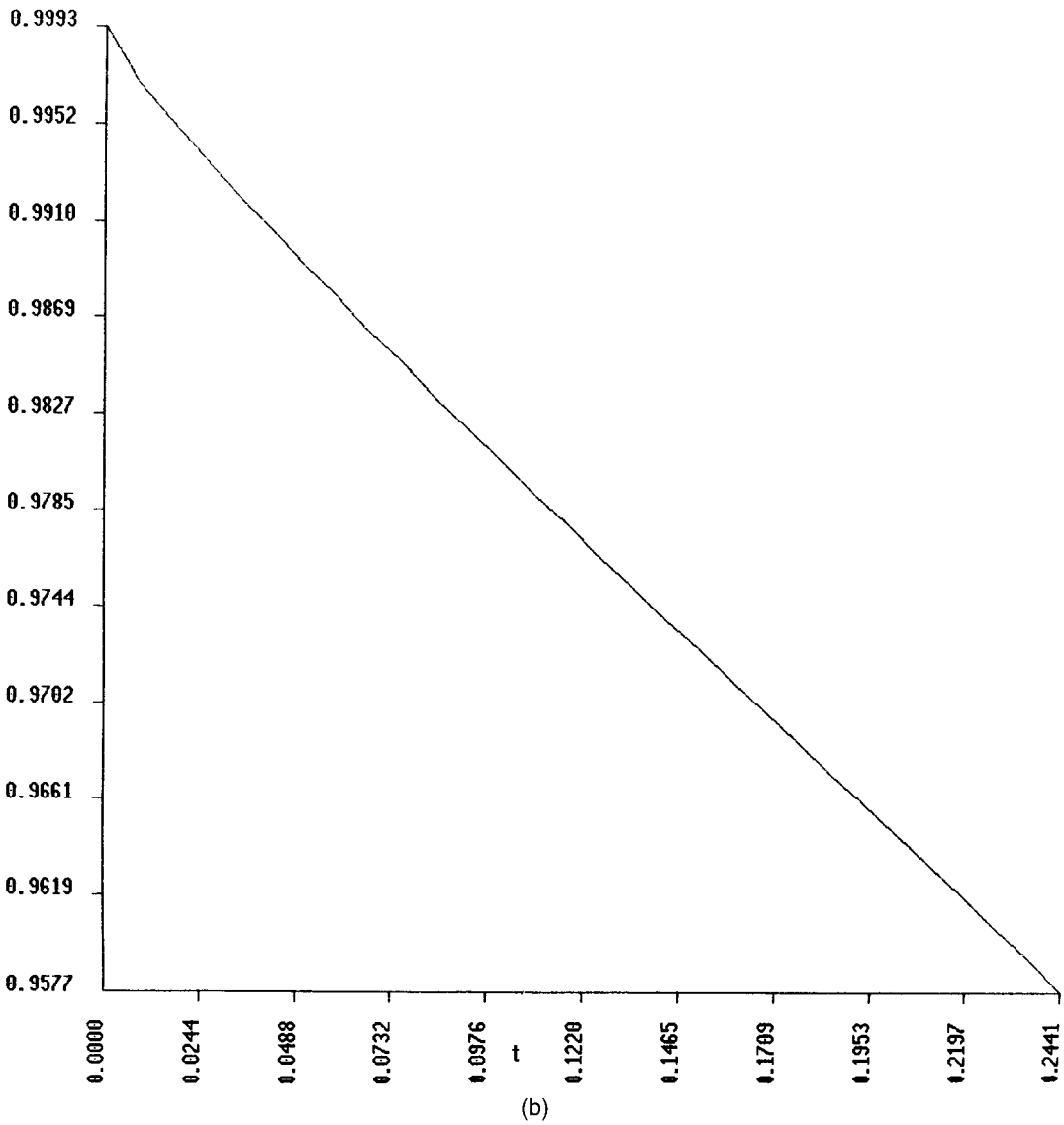


**FIGURE 5.** (Continued)

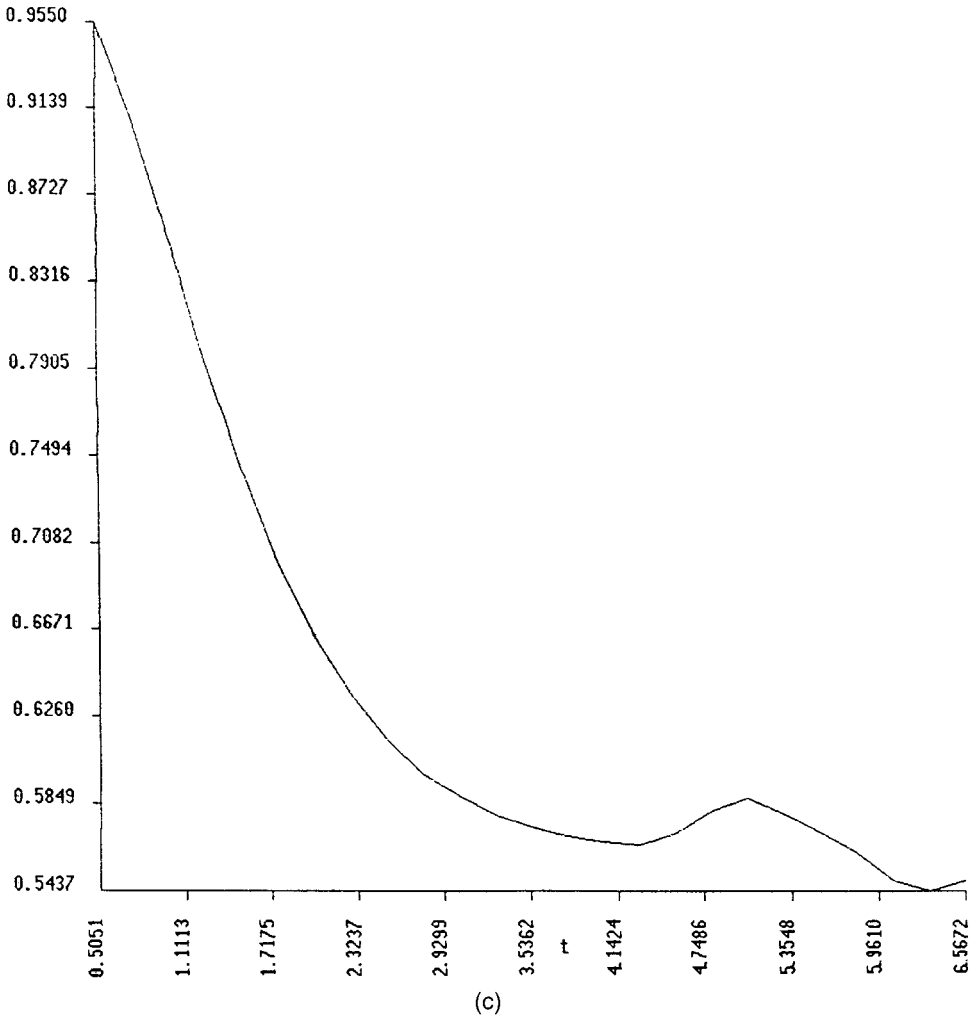


**FIGURE 5.** (Continued)

high intensity and a large number of photons. For example, even for a laser of intensity as low as $1 \times 10^{-3}$ W cm$^{-2}$ with $\hbar\omega = 1$ eV, the number of photons present in the unit coherence volume is $\cong 2 \times 10^5$. Thus, a high-intensity laser perturbs the system strongly and multiphoton phenomena occur causing, for example, rapid excitation. Our results confirm this. For example, at $t = 0$, when the field is zero, $P_{\text{g.s.}} = 1$. With increase in time, the field builds and, hence, the excitation probability increases. Thus, we observe that at $t = 0.25$ au excitation ($P_{\text{g.s.}} = 0.9577$) is already taking place with no ionization. Afterward, progressive excitation opens up a number of routes for ionization. For example, at $t = 6.361$ au, $P_{\text{g.s.}} = 0.5437$ ($\cong 46\%$ excitation). In other words, a large number of excited states become mixed in the TD density even at $t = 6.361$ au. Figures 6 and 7 depict the magnetic susceptibility and electric polarizability, respectively, both of which also show nonlinear oscillations faster than the laser field.

Figure 8(a)–(f) depicts the space–time nonlinear oscillations of the 3-D electron density [the position of the stationary He nucleus is shown by a cross in Fig. 8(a)] as a function of $x(x^2 = \tilde{\rho})$ and $\tilde{z}$. It is clear that the oscillating atom is gradually losing electron density. The plots are $\tilde{\rho}$-symmetric, but, as time progresses, they develop a pronounced $\tilde{z}$-asymmetry which keeps on switching from left to right because of the $\tilde{z}$-polarized laser field. The geometry of this electron loss can be seen more clearly from the difference–density ($\Delta\rho$)

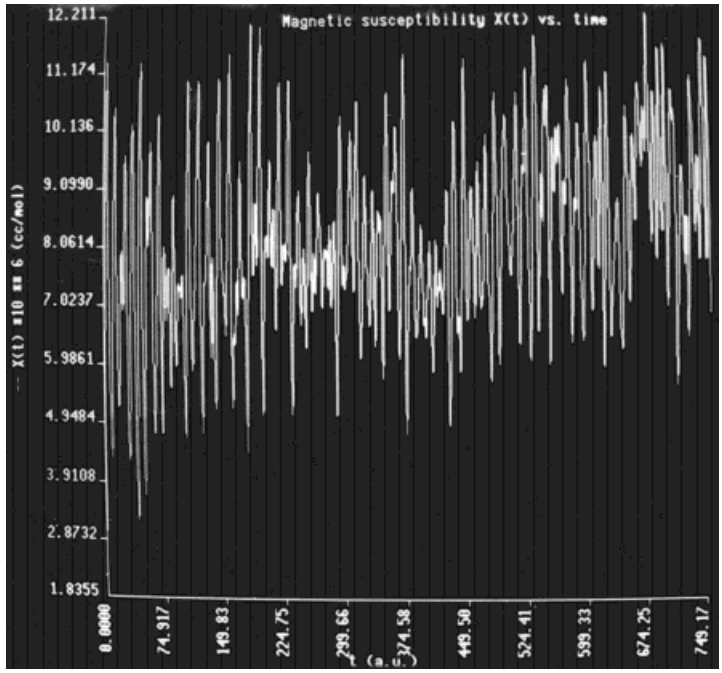


**FIGURE 6.** TD, nonlinearly oscillating magnetic susceptibility, $\chi(t)$, positive values, plotted against time, in au. The oscillation amplitude first increases and then decreases due to progress in ionization.

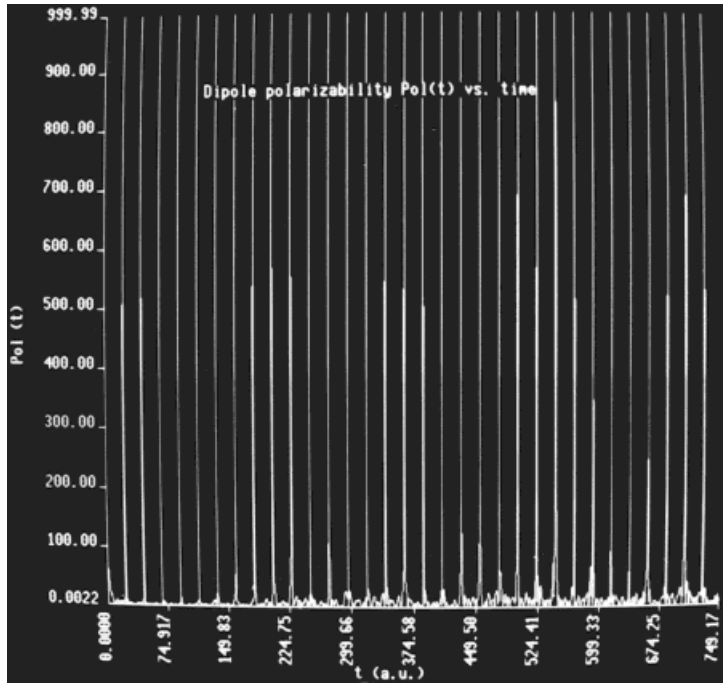


**FIGURE 7.** TD, nonlinearly oscillating polarizability, $\mathrm{Pol}(t) = P_{\hat{z}\hat{z}}(t)$, plotted against time, in au. Values above 1000 have been truncated in the plot.

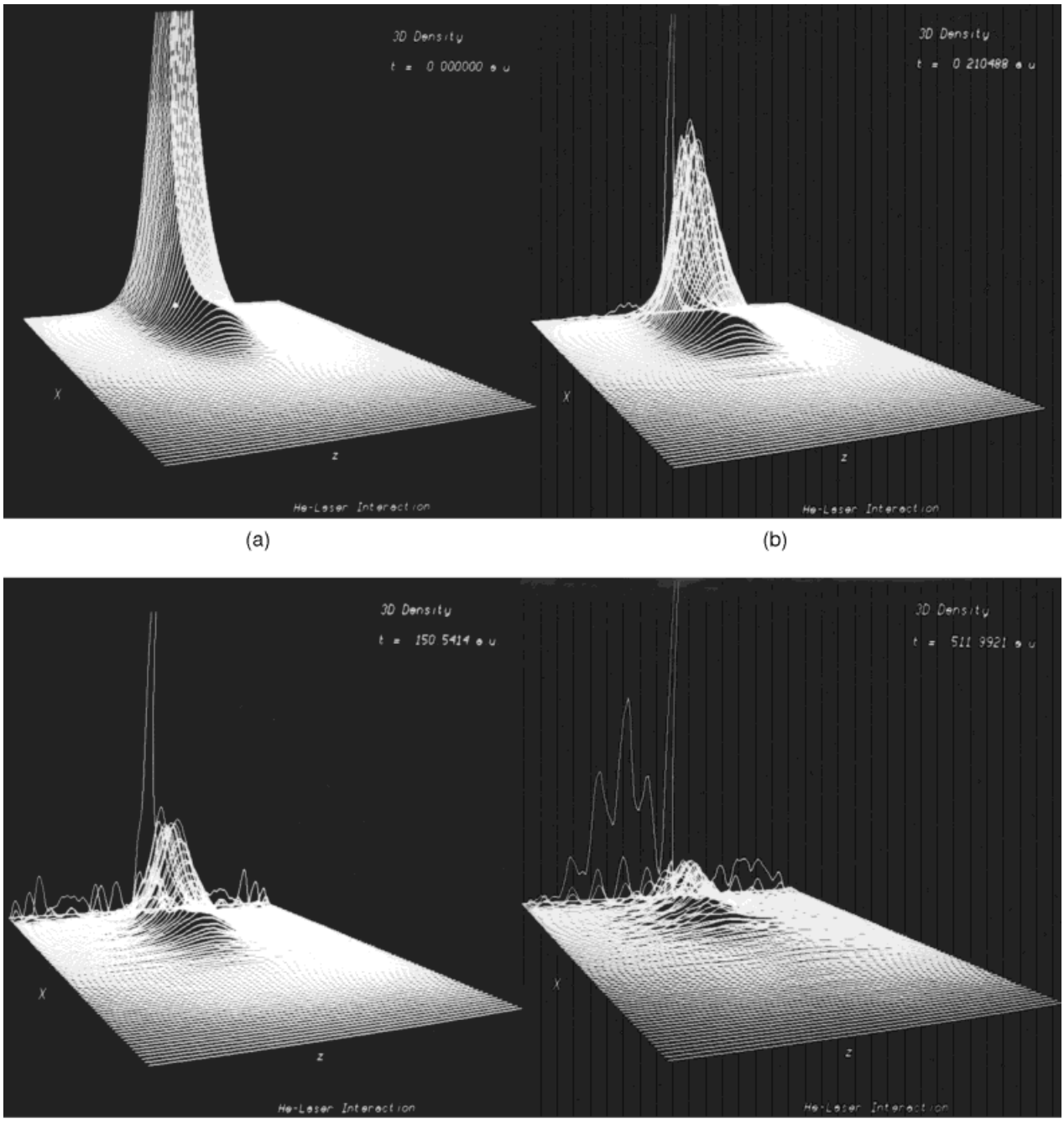


**FIGURE 8.** Perspective plots of the TD density, $\rho(\tilde{\rho}, \tilde{z}, t)$, corresponding to the $x\tilde{z}$ $(x^2 = \tilde{\rho})$ plane. The He nucleus is shown by a cross: (a) $t = 0.0$; (b) $t = 0.210488$; (c) $t = 150.5414$; (d) $t = 511.9921$; (e) $t = 750.4335$ au.

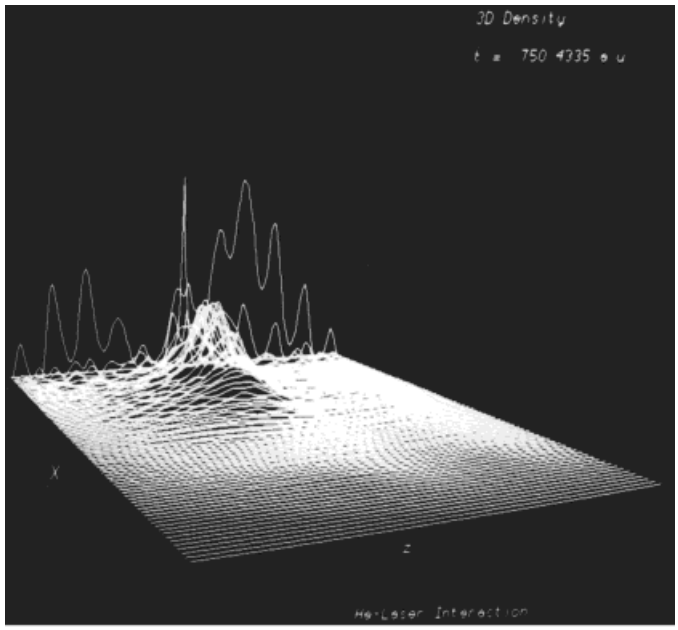


(e)

**FIGURE 8.** (Continued)

plots [Fig. 9(a)–(e)]. In the course of time, $\Delta\rho$ shows a number of maxima on both sides of $\tilde{z}$ and a triple minimum around the He nucleus for $\tilde{\rho}$ close to zero. All the peaks and their relative heights as well as all the troughs and their relative depths oscillate in response to the laser field. $\Delta\rho$ gradually spreads itself in the grid, its amplitude of oscillation increasing. This indicates a continuing depletion in the $1s$ contribution to the density and increase in higher $s$, $p$, $d$, etc., contributions. Thus, in the time-evolved density, one can identify many states of He*, He** (autoionizing), $He^+$, and the continuum, with relative percentages of mixing [64]. Transitions between such states are responsible for photoemission by the system (see later).

Figure 10(a)–(f) depicts the pulsating potential, $v_{eff}(\rho; \mathbf{r}, t)$, as a function of $x$ and $\tilde{z}$, in the course of time; $v_{eff}$ displays a number of peaks/valleys whose heights/depths and separations oscillate nonlinearly. These peaks and valleys occur due to the fluctuating interaction between the positive and negative density-dependent terms in $v_{eff}$ [Eq. (10)]. Thus, the *cobra-hood* potential at $t = 0$ lowers its hood and widens its neck ($v_{eff} \to -\infty$ at the nuclear site) as time progresses (He nucleus at the position marked by a cross). It also develops an intricate pattern of valleys on both sides along $\tilde{z}$ away from the He nucleus. Electron density tends to gravitate toward these valleys, leading to positive $\Delta\rho$ (see Fig. 9). The $\Delta v_{eff}$ plots in Figure 11(a)–(e) show the space–time changes in the effective potential surface on which the given process occurs. Note that after some time $\Delta v_{eff}(\rho; \mathbf{r}, t)$ maintains a characteristic shape in spite of its pulsations. Since the laser field is $\tilde{z}$-polarized, the potential structure is more intricate and fluctuating along the $\tilde{z}$-direction than is the structure along the $\tilde{\rho}$-direction which does not change drastically.

An indication of the nature of the fluid flow of the electron density can be obtained from the negative flux, $-\nabla \cdot (\rho \nabla \chi) = \partial\rho/\partial t$ [Eq. (5)]. This is depicted in Figure 12(a)–(e). As time progresses, the fluid motion spreads more and more over the grid, with increasingly complicated patterns. Thus, Figures 8–12 provide us a detailed visual understanding of the nature of the interaction in terms of fluid flow, excitation, and ionization as observed through changes in $\rho$ and $v_{eff}$.

We now consider the phenomenon of photoemission by the atom under the laser field. Figures 13 and 14 depict the power and the rate spectrum, respectively, for photoemission, corresponding to $t = 517.29647$ au, that is, 12.512833 fs. Based on Figures 13 and 14 as well as the unscrambling of $\rho(\mathbf{r}, t)$ in terms of He*, He**, $He^+$, and continuum states [64], Table I shows the dom-

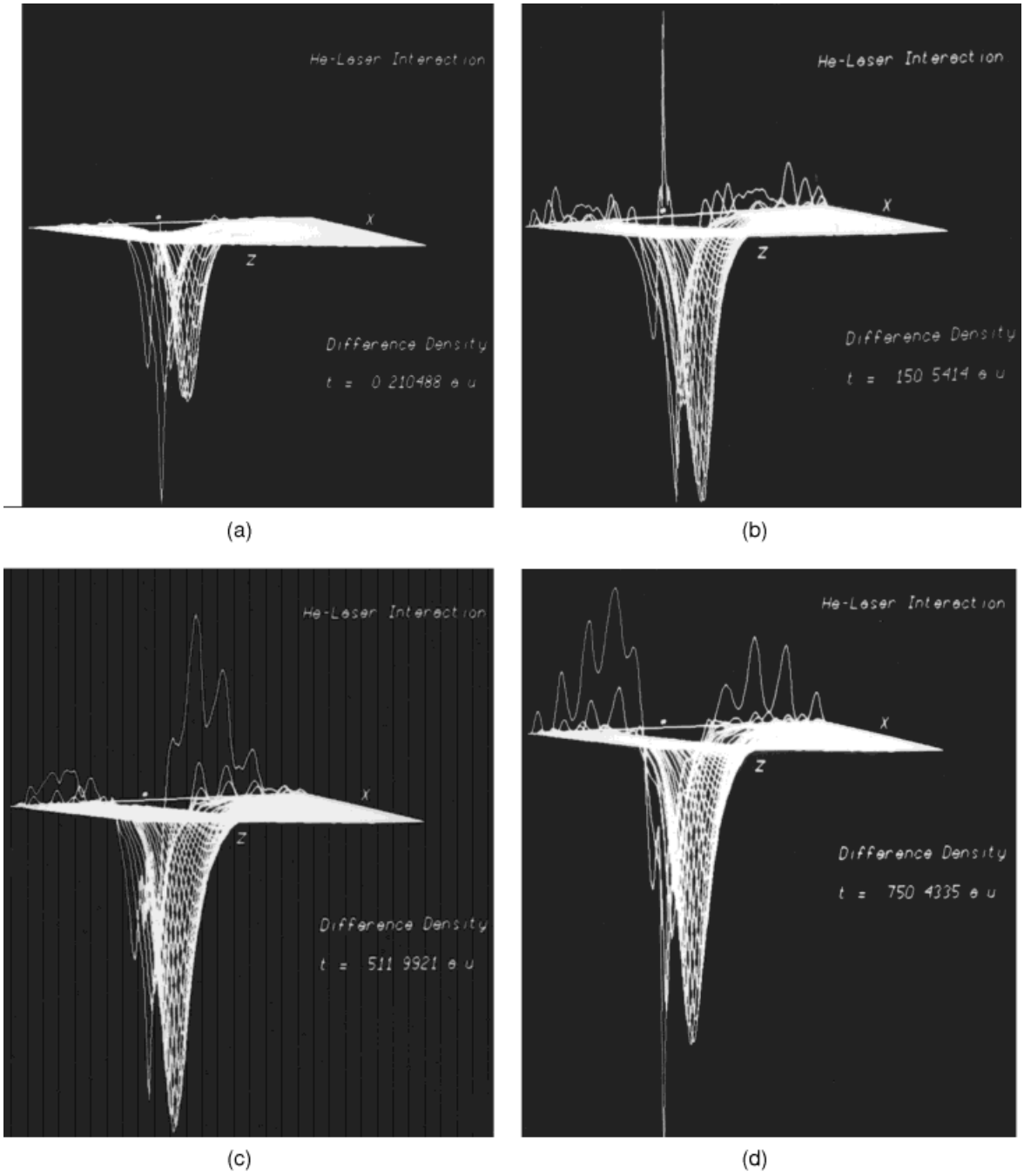


**FIGURE 9.** Perspective plots of the TD difference density $\Delta\rho(\tilde{\rho}, \tilde{z}, t)$, corresponding to the $x\tilde{z}(x^2 = \tilde{\rho})$ plane. The He nucleus is shown by a cross. Positive $\Delta\rho$ values are above the $x\tilde{z}$ plane, while negative $\Delta\rho$ values are below. (a) $t = 0.210488$; (b) $t = 150.5414$; (c) $t = 511.9921$; (d) $t = 750.4335$ au.

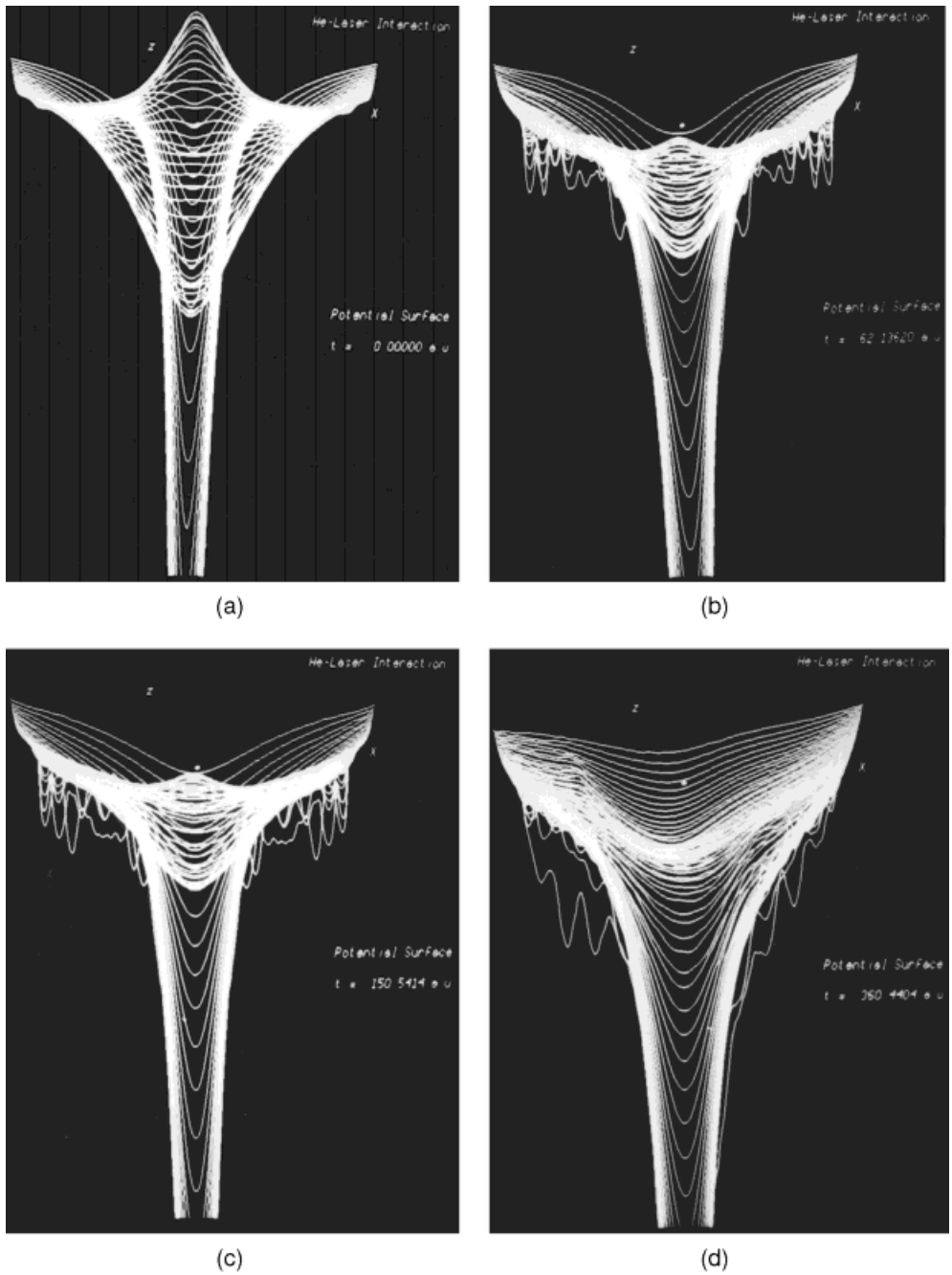


**FIGURE 10.** Perspective plots of the *cobra-hood* TD effective potential surface $v_{eff}(\tilde{\rho}, \tilde{z}, t)$ corresponding to the $x\tilde{z}$ ($x^2 = \tilde{\rho}$) plane. Note the gradual lowering of the hood, swelling of the neck, and development of an intricate structure. The He nucleus is shown by a cross. (a) $t = 0.0$; (b) $t = 62.13620$; (c) $t = 150.5414$; (d) $t = 360.4404$; (e) $t = 511.9921$; (f) $t = 750.4335$ au.

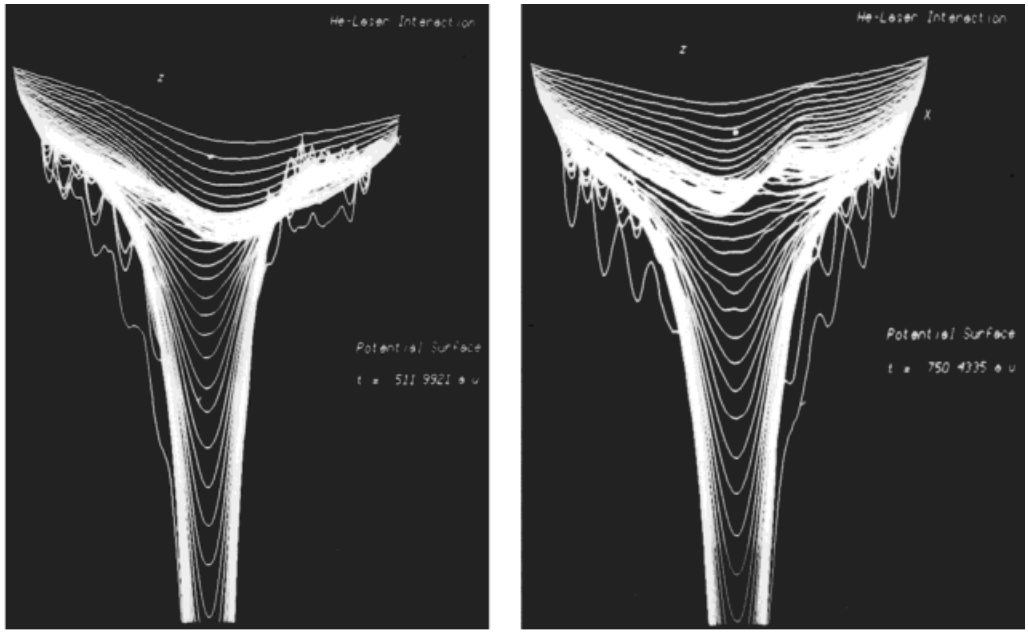


**FIGURE 10.** (Continued)

inant spectral transitions responsible for photoemission, corresponding to the mechanistic routes a–k, except high harmonic generation which is shown separately in Table II. Profuse single-photon, multiphoton, and usual dipole-forbidden transitions occur. From Table I, route a appears to be the most dominant at this time, followed by routes b, d, and i. In other words, the most significant bound state and resonance state transitions involve those from He* to He (g.s.) and from He** (higher) to He** (lower). The most significant continuum transitions are from the continuum to He**. Continuum–continuum transitions corresponding to route k overlap on the entire range of frequencies studied (a practical upper limit of the continuum energy at this time is 12.32839 au). Some of the labeled resonance peaks in Figures 13 and 14 are identified in Table I, column 1, through a matching between the calculated and experimental transition frequencies. Other peaks have not been identified.

It is well known that the characteristics of radiation emitted by atomic systems become strongly affected [66, 67] under laser fields, for example, usual dipole-forbidden transitions occur frequently in the power spectrum; these are produced by the weakening of selection rules (both single- and multiphoton). Assuming an adiabatic evolution, that is, $\hat{\mathscr{L}}(t + n\Delta t) = \hat{\mathscr{L}}(t + (n-1)\Delta t)$ [see Eq. (32)], the hydrodynamical density $\rho(\mathbf{r}, t)$ contains a mixture of many unperturbed He and $He^+$ state densities. Such mixing occurs due to the absorption of photon energy leading to transitions to various states.

Emissions involving transitions of two electrons (with dipole selection rules as $\Delta S = 0$, $\Delta L = 0, \pm 1$ and $\Delta J = 0, \pm 1$) are found to be (see Table I: routes c, d, and e) of low-power spectral density, except $2s^2(^1S) \leftarrow 2p^2(^1S)$, $2s^2(^1S) \leftarrow 23sp(-)(^1P^0)$, $2s^2(^1S) \leftarrow 3d5d(^1G)$ and $2s^2(^1S) \leftarrow 38sp(+)(^1P^0)$ for which the PSD values are 1.08075, 1.44417, 2.27390, and 3.41787, respectively. We see that the transition $2s^2(3^1S) \leftarrow 3d5d(^1G)$ is spin-allowed but $L$- and $J$-forbidden, while the other two-electron emissions mentioned above are allowed.

We now explain the mechanism of photoemission from different possible routes as discussed below. Disregarding route k, the following are the frequency ranges for the dominant transitions according to routes a–j in Table I:

(i) $0.01214 \leq \omega \leq 0.49799$ Route g
(ii) $0.08502 \leq \omega \leq 0.77736$ Route i
(iii) $0.12146 \leq \omega \leq 0.17005$ Route b

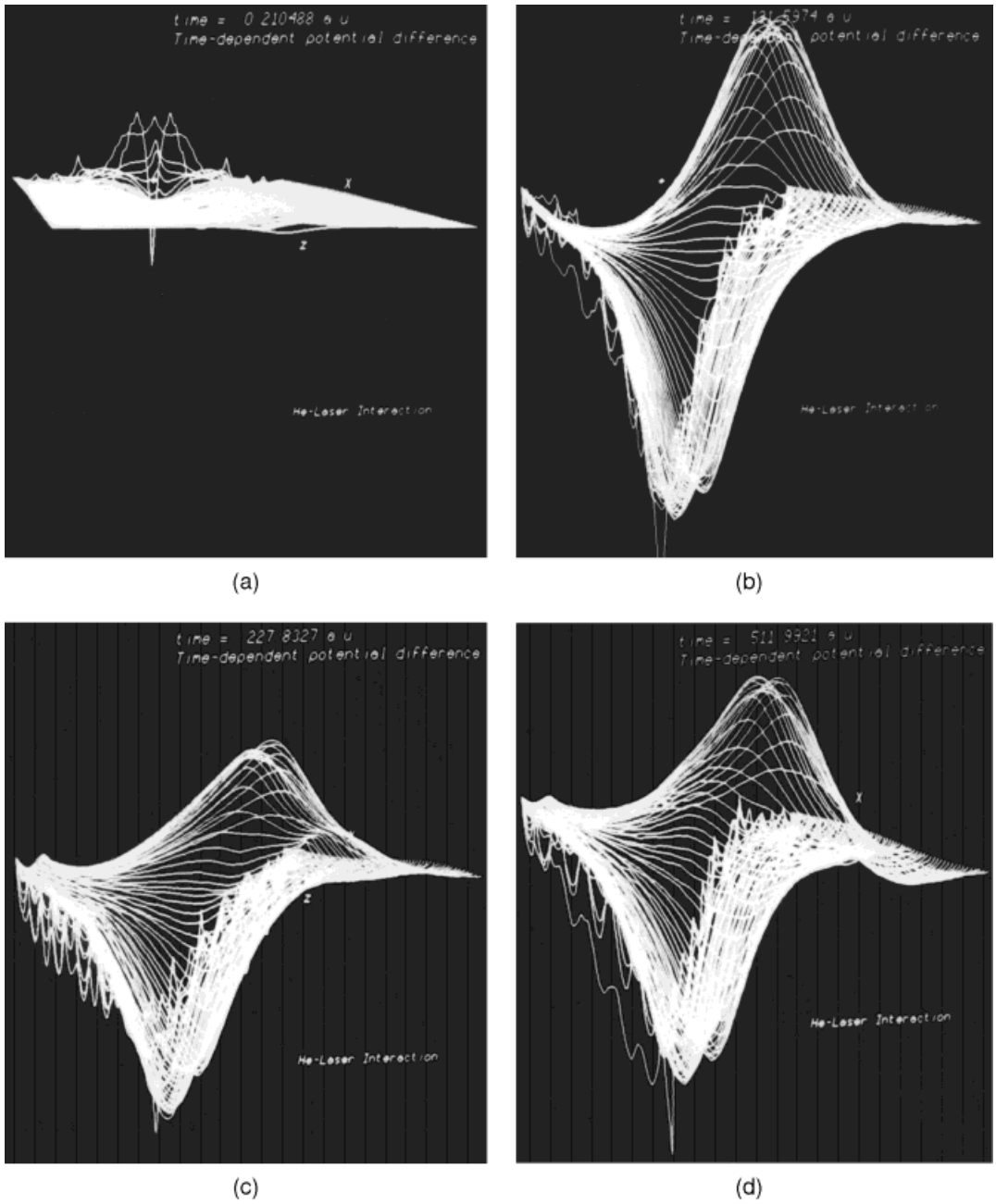


**FIGURE 11.** Perspective plots of the effective difference potential $\Delta v_{eff}(\tilde{\rho}, \tilde{z}, t)$ corresponding to the $x\tilde{z}$ $(x^2 = \tilde{\rho})$ plane. The He nucleus is shown by a cross. Positive $\Delta v_{eff}$ values are above the $x\tilde{z}$ plane while negative values are below. (a) $t = 0.210488$; (b) $t = 131.5974$; (c) $t = 227.8327$; (d) $t = 511.9921$; (e) $t = 750.4335$ au.

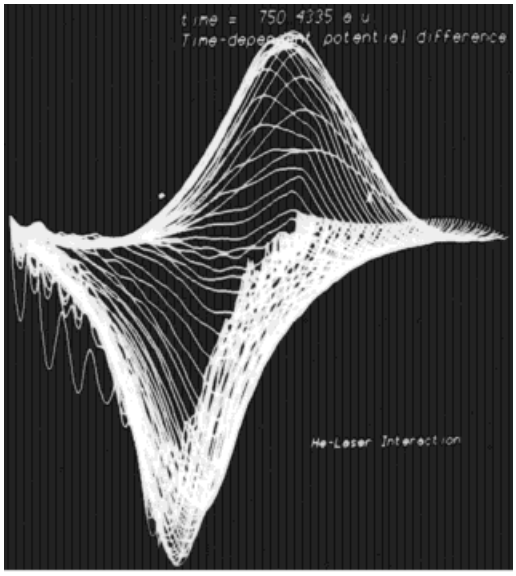


(e)

**FIGURE 11.** (Continued)

(iv) $0.15790 \leq \omega \leq 0.69233$ Route d
(v) $0.71663 \leq \omega \leq 0.89882$ Route a
(vi) $1.22677 \leq \omega \leq 2.08915$ Route e
(vii) $1.49398 \leq \omega \leq 1.99197$ Route f
(viii) $2.00412 \leq \omega \leq 2.17417$ Route j
(ix) $2.12558 \leq \omega \leq 2.38065$ Route c
(x) $2.92723 \leq \omega \leq 3.58312$ Route h

It may be noted that the helium ground-state energy, first ionization threshold, and the second ionization threshold are taken, respectively, as $-2.9037244$ [68], $-1.9997188$, and 0.0 au. The singly excited (bound) states occur between the first two energy levels, whereas the doubly excited (autoionizing) states occur between the last two values. Apart from the above transitions, there is a range $0.91096 \leq \omega \leq 1.21462$ whose PSD($\omega$) and RSD($\omega$) are comparable to those for route e. These may be interpreted as continuum–continuum transitions as well as those between ''dressed'' states. Table II shows that at $t = 12.512833$ fs high harmonic generation from $n = 3$–21 is observed, with $9\omega_L$ having the most favorable combination of PSD($\omega$) and RSD($\omega$). The weak higher harmonics are because of relatively smaller contributions of electrons returning to the ground state of the He atom from the continuum at this stage of the time evolution. Note that the relative importance of different routes as well as the high-order harmonics will change if evolution is carried out to the asymptotic time limit. However, we feel that the most significant physical effects necessary to explain the mechanism of photoemission have already revealed themselves at $t \cong 750$ au (3000 time steps). It is conceivable that, for atom–laser interactions in general, PSD($\omega$) and RSD($\omega$) might manifest quantum chaos due to transitions between a large number of continuum states and closely spaced states lying just below the ionization threshold(s). The total PEC [Eq. (105)] is 166.29 au = 46.46 Å$^2$.

Recently, Gross et al. [69–73] developed a TD DFT for studying the interactions between many-electron atoms and intense laser fields. For an $N$-electron atom, this requires the solution of $N$ TD Kohn–Sham (KS) equations to obtain $N$ TDKS orbitals, subject to a local, TD XC potential. The XC potential is approximated through a TD formulation of the optimized potential method (OPM) [74] to obtain $v_{xc}(\mathbf{r}, t)$ rather than $v_{xc}[\rho(\mathbf{r}, t)]$. The local effective potential in the TDKS equations is to be determined such that the calculated TDKS orbitals make a total action functional stationary. Following the so-called KLI [75] simplified approach to the rather difficult OPM, Gross et al. [69–73] proposed a method to obtain an approximate XC potential as an explicit functional of the $N$ TDKS orbitals. The method has been applied, in the exchange-only approximation, to He, Be, and Ne (valence electrons only) atoms under intense laser fields over about 40 optical cycles in order to study (i) their ionization through the respective numbers of electrons in different orbitals as well as the populations of the singly and multiply charged cationic species as functions of time, and (ii) high-order harmonic generation via the Fourier transform of the TD induced dipole moment. By normalizing the experimental harmonic spectral data to a particular (e.g., the 33rd order) calculated harmonic and by a superposition of the calculated harmonics from more than one laser intensity, Gross et al. obtained a satisfactory matching between the calculated and observed high-order harmonic distributions. The present work has not yet dealt with the nonlinear optical problems of propagation and mixing of the harmonics which are essential for a comparison with experimental results. The present work (see also [64, 65, 76]) attempts a parallel development in TD-DFT in that it requires one to solve only a single TD equation

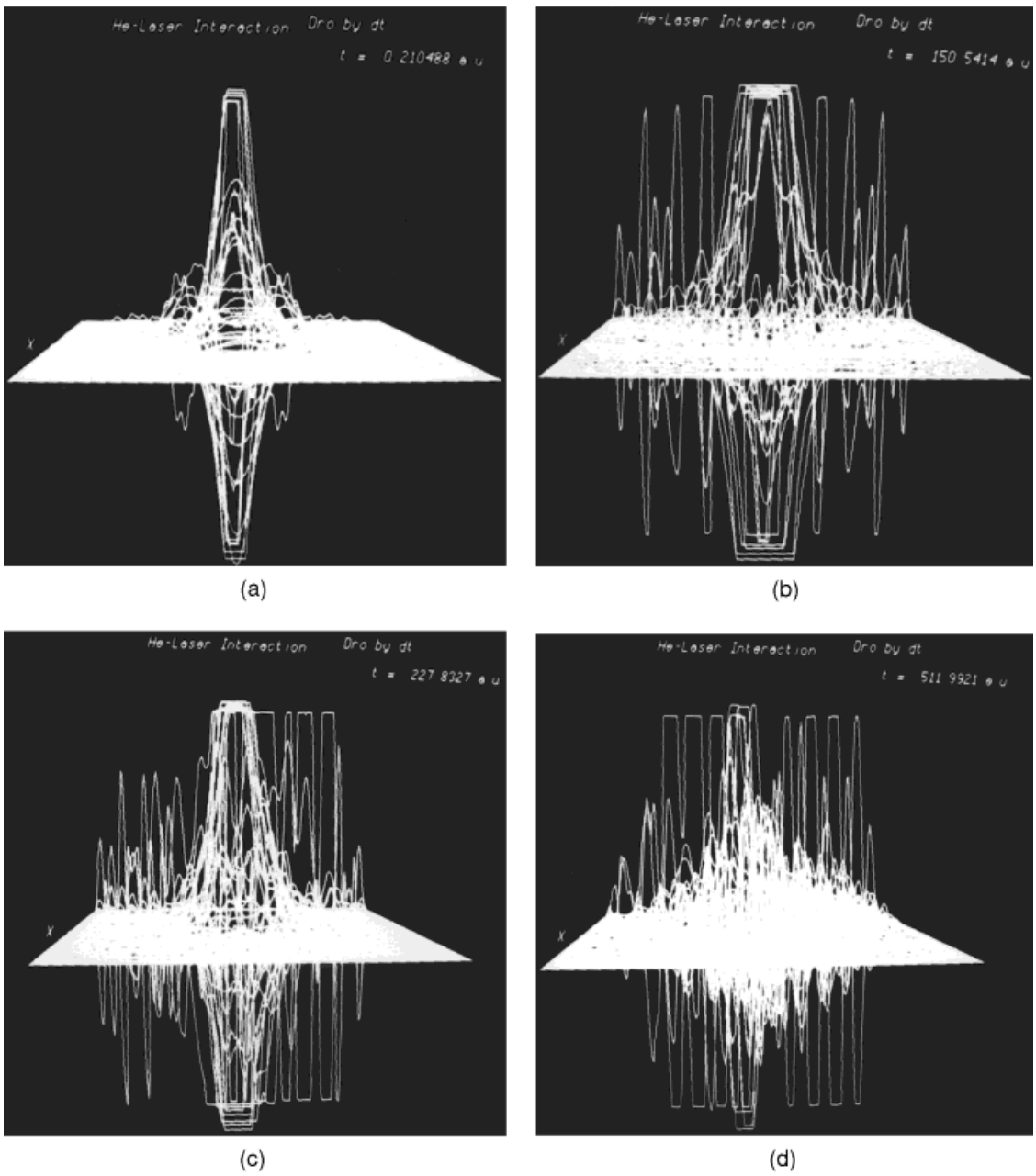


**FIGURE 12.** Perspective plots of the TD negative flux, $(-\nabla \cdot \mathbf{J})$, corresponding to the $x\tilde{z}$ $(x^2 = \tilde{\rho})$ plane. The He nucleus is at the midpoint of the shortest horizontal line. (a) $t = 0.210488$; (b) $t = 150.5414$; (c) $t = 227.8327$; (d) $t = 511.9921$; (e) $t = 750.4335$ au.

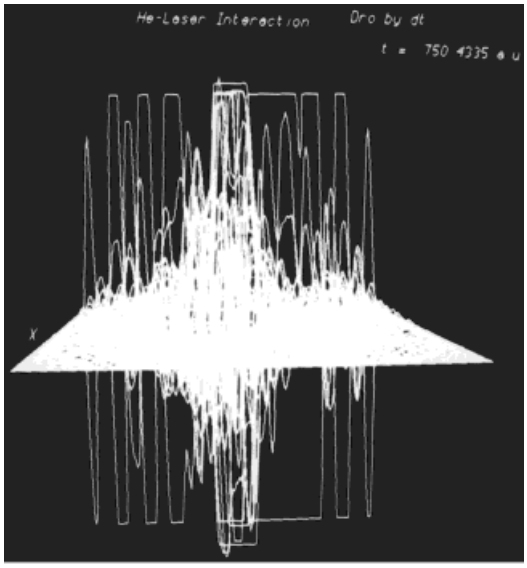


(e)

**FIGURE 12.** (Continued)

of motion [Eq. (18)] for many-electron systems, obtained from quantum fluid dynamics [41], which provide the foundations for all TD-DFT approaches. Equation (18) involves the XC potential $v_{xc}[\rho(\mathbf{r}, t)]$ for which a Dirac–Wigner combined functional has been presently adopted. However, this single-equation approach, which yields a single hydrodynamical function (whose modulus-square gives the electron density) for an $N$-electron system, depends on the availability of a satisfactory $T^{corr}[\rho]$ [see Eq. (18)]. For a general many-electron system, this problem has not yet been solved, although it ought to be simpler to deal with in the case of noble gas atoms [48].

## Conclusion

Despite its apparent simplicity, the quantum fluid dynamical approach which involves TD-DFT and studies the evolution of a dynamical system/process in real time in terms of a single equation in 3-D space, has the potential to emerge as a useful, comprehensive method for studying TD phenomena from start to finish, including atomic/molecular scattering and molecular reaction dynamics. For the atom–laser interaction studied in this article, our analysis attempts to obtain a wealth of detailed information and insight concerning the interlinked phenomena of photoionization and photoemission (including high harmonic generation), based on the evolution *up to a particular time*,

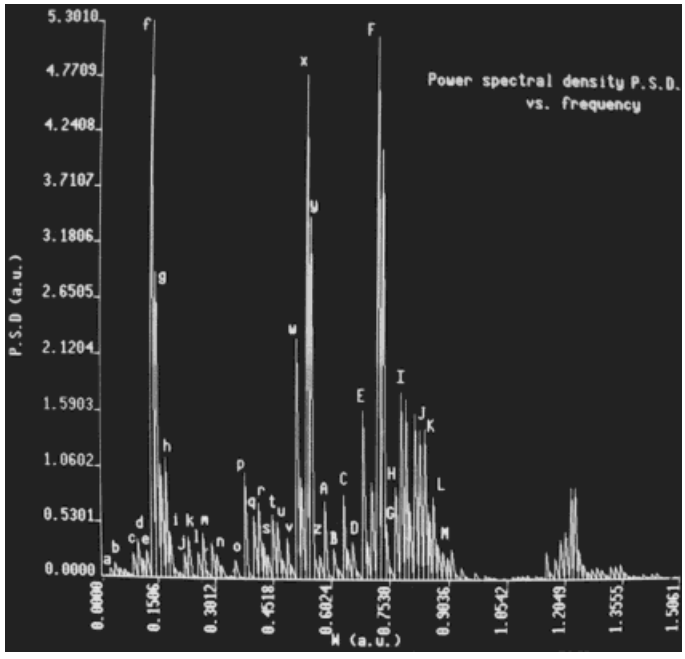


**FIGURE 13.** Power spectral density, PSD($\omega$), for photoemission plotted against emission frequency ($\omega$), in au. Resonance peaks marked by upper-case letters correspond to routes a and d, while those marked by lower-case letters correspond to routes b, d, and g (see Table I).

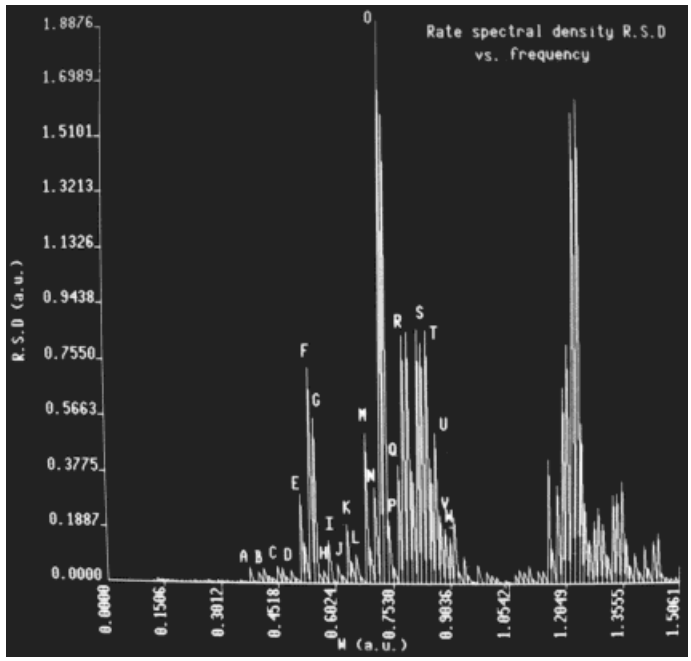


**FIGURE 14.** Rate spectral density, RSD($\omega$), for photoemission plotted against emission frequency ($\omega$), in au. Resonance peaks marked by upper-case letters correspond to routes a, d, and g (see Table I).

**TABLE I**

**Frequency ($\omega$), PSD($\omega$), and RSD($\omega$) at $t = 517.29647$ au (12.512833 fs), for the dominant transitions responsible for photoemission at this time excluding high harmonic generation ($n\omega_L$, Table II), according to the mechanistic routes a–k.**

| $\omega$ (Label in Figs. 13 and 14) | Transitions | PSD($\omega$) | % Total PSD | RSD($\omega$) | % Total RSD |
|---|---|---|---|---|---|
| I. Route a | | | | | |
| 0.74092($G, P$) | $1s^2 \leftarrow 1s2s(^1S)$ | 0.53130 | 0.738 | 0.21610 | 0.0018 |
| 0.77736($I, R$) | $1s^2 \leftarrow 1s2p(^1p)$ | 1.77318 | 2.464 | 0.83294 | 0.0070 |
| 0.83809($K, T$) | $1s^2 \leftarrow 1s3s(^1S)$, $1s3p(^1P)$, $1s3d(^1D)$ | 1.43729 | 1.998 | 0.84608 | 0.0071 |
| 0.86238($L, U$) | $1s^2 \leftarrow 1s4p(^1P)$, $1s4d(^1D)$, $1s4f(^1F)$ | 0.78707 | 1.094 | 0.50479 | 0.0042 |
| 0.87453($M, V$) | $1s^2 \leftarrow 1s5s(^1S)$, $1s5p(^1P)$ | 0.34436 | 0.479 | 0.23032 | 0.0019 |
| 0.85023 | $1s^2 \leftarrow 1s4s(^1S)$ | 0.63550 | 0.883 | 0.39060 | 0.0033 |
| 0.88667 | $1s^2 \leftarrow 1s7s(^1S)$, $1s7p(^1P)$ | 0.26541 | 0.369 | 0.18502 | 0.0015 |
| 0.89882 | $1s^2 \leftarrow 1s14s(^1S)$, $1s21p(^1P)$ | 0.21638 | 0.301 | 0.15712 | 0.0013 |

(Continued)

**TABLE I**
**(Continued)**

| $\omega$ (Label in Figs. 13 and 14) | Transitions | PSD($\omega$) | % Total PSD | RSD($\omega$) | % Total RSD |
|---|---|---|---|---|---|
| II. Route b | | | | | |
| 0.12146($e$) | $1s2s(^1S) \leftarrow 1s5s(^1S)$ | 0.25781 | 0.358 | 0.00046 | 0.386E-05 |
| III. Route c | | | | | |
| 2.12558 | $1s^2 \leftarrow 2s^2(^1S)$ | 6.425E-03 | 8.930E-03 | 0.06171 | 0.516E-03 |
| 2.21060 | $\begin{cases} 1s^2 \leftarrow 2p^2(^1D), \\ 2s2p(^1P^0) \end{cases}$ | 0.225E-03 | 0.310E-03 | 0.00243 | 0.203E-04 |
| 2.28348 | $1s^2 \leftarrow 2p^2(^1S)$ | 0.490E-04 | 0.681E-04 | 0.00058 | 0.488E-05 |
| 2.30777 | $1s^2 \leftarrow 23sp(-)(^1P^0)$ | 0.436E-03 | 0.610E-03 | 0.00536 | 0.448E-04 |
| 2.31990 | $1s^2 \leftarrow 2s3s(^1S)$ | 1.615E-03 | 0.220E-03 | 0.02017 | 0.169E-03 |
| 2.33207 | $1s^2 \leftarrow 2p3p(^1D)$ | 0.697E-04 | 0.969E-04 | 0.00088 | 0.739E-05 |
| 2.34422 | $1s^2 \leftarrow 2p3d(^1D^0)$ | 1.279E-03 | 1.780E-03 | 0.01648 | 0.138E-03 |
| 2.36850 | $1s^2 \leftarrow 3d3d(^1G)$ | 0.249E-03 | 0.350E-03 | 0.00330 | 0.276E-04 |
| 2.38065 | $1s^2 \leftarrow 3p5d(^1D)$ | 0.579E-03 | 0.810E-03 | 0.00782 | 0.653E-04 |
| IV. Route d | | | | | |
| 0.15790 | $2s^2(^1S) \leftarrow 2p^2(^1S)$ | 1.08075 | 1.502 | 0.00425 | 0.356E-04 |
| 0.17004($h$) | $2s^2(^1S) \leftarrow 23sp(-)(^1P^0)$ | 1.14417 | 1.590 | 0.00563 | 0.470E-04 |
| 0.23077($k$) | $2s^2(^1S) \leftarrow 2p3p(^1D)$ | 0.38984 | 0.542 | 0.00479 | 0.400E-04 |
| 0.30365($n$) | $2s3s(^1S) \leftarrow 3s4s(^1S)$ | 0.23019 | 0.320 | 0.00645 | 0.539E-04 |
| 0.40082($q$) | $2s2p(^1P) \leftarrow 3s^2(^1S)$ | 0.60100 | 0.835 | 0.03870 | 0.323E-03 |
| 0.51014($w$, $E$) | $2s^2(^1S) \leftarrow 3d5d(^1G)$ | 2.27390 | 3.160 | 0.30188 | 0.252E-02 |
| 0.54658($y$, $G$) | $2s^2(^1S) \leftarrow 38sp(+)(^1P^0)$ | 3.41787 | 4.750 | 0.55810 | 0.466E-02 |
| 0.57087($z$, $H$) | $2s^2(^1S) \leftarrow 4s^2(^1S)$ | 0.23010 | 0.320 | 0.04281 | 0.358E-03 |
| 0.58301($A$, $I$) | $2s^2(^1S) \leftarrow 4s4p(^1P^0)$ | 0.74503 | 1.035 | 0.14764 | 0.123E-02 |
| 0.63160($C$, $K$) | $2s^2(^1S) \leftarrow 5s^2(^1S)$ | 0.80818 | 1.123 | 0.20363 | 0.170E-02 |
| V. Route e | | | | | |
| 1.28750 | $1s3s(^1S) \leftarrow 2s^2(^1S)$ | 0.11963 | 0.166 | 0.25533 | 0.00213 |
| 1.43325 | $1s2p(^1P) \leftarrow 2s2p(^1P)$ | 0.04853 | 0.0675 | 0.14289 | 0.00119 |
| VI. Route f($n_{\text{lower}} \leftarrow n_{\text{upper}}$) | | | | | |
| 1.49398 | $1 \leftarrow 2$ | 0.00506 | 0.704E-02 | 0.01688 | 0.141E-03 |
| 1.77334 | $1 \leftarrow 3$ | 0.00575 | 0.799E-02 | 0.03206 | 0.268E-03 |
| 1.87050 | $1 \leftarrow 4$ | 0.02014 | 2.799E-02 | 0.13181 | 0.110E-02 |
| 1.91909 | $1 \leftarrow 5$ | 0.01427 | 1.984E-02 | 0.10089 | 0.843E-03 |
| 1.94339 | $1 \leftarrow 6$ | 0.00149 | 0.207E-02 | 0.01093 | 9.914E-05 |
| 1.95550 | $1 \leftarrow 7$ | 0.00557 | 0.774E-02 | 0.04166 | 0.348E-03 |
| 1.96768 | $1 \leftarrow 8$ | 0.00611 | 0.849E-02 | 0.04652 | 0.389E-03 |
| 1.97983 | $1 \leftarrow 9$ | 0.00239 | 0.332E-02 | 0.01856 | 0.155E-03 |
| 1.99197 | $1 \leftarrow 15$ | 0.00436 | 0.605E-02 | 0.03443 | 0.288E-03 |
| VII. Route g($n_{\text{lower}} \leftarrow n_{\text{upper}}$) | | | | | |
| 0.01214 | $6 \leftarrow 7$ | 0.00585 | 0.813E-02 | $\cong 10^{-8}$ | $\cong$ 1.0E-10 |
| 0.02429($a$) | $5 \leftarrow 6$ | 0.07690 | 0.107 | 0.110E-05 | $\cong$ 1.0E-08 |
| 0.03644($b$) | $5 \leftarrow 7$ | 0.13392 | 0.186 | 0.648E-05 | $\cong$ 1.0E-07 |
| 0.04858 | $4 \leftarrow 5$ | 0.08193 | 0.114 | 0.940E-05 | $\cong$ 1.0E-07 |

(Continued)

**TABLE I**
**(Continued)**

| $\omega$ (Label in Figs. 13 and 14) | Transitions | PSD($\omega$) | % Total PSD | RSD($\omega$) | % Total RSD |
|---|---|---|---|---|---|
| VII. Route g($n_{\text{lower}} \leftarrow n_{\text{upper}}$) | | | | | |
| 0.06073 | 4 ← 6 | 0.06818 | 0.948E-01 | 0.153E-04 | ≅ 1.0E-07 |
| 0.07287 | 5 ← 15 | 0.03395 | 0.472E-01 | 0.131E-04 | ≅ 1.0E-07 |
| 0.08502($c$) | 4 ← 7 | 0.23186 | 0.322 | 0.143E-03 | 0.119E-05 |
| 0.09717($d$) | 3 ← 4 | 0.36612 | 0.509 | 0.336E-03 | 0.281E-05 |
| 0.10932 | 4 ← 9 | 0.18029 | 0.251 | 0.236E-03 | 0.197E-05 |
| 0.18219($i$) | 3 ← 7 | 0.43540 | 0.605 | 0.263E-02 | 0.220E-04 |
| 0.19434 | 3 ← 8 | 0.09152 | 0.127 | 0.672E-03 | 0.561E-05 |
| 0.20649 | 3 ← 10 | 0.05136 | 0.714E-01 | 0.452E-03 | 0.378E-05 |
| 0.21863($j$) | 3 ← 13 | 0.24066 | 0.334 | 0.251E-02 | 0.210E-04 |
| 0.27936 | 2 ← 3 | 0.06820 | 0.948E-01 | 0.149E-02 | 0.124E-04 |
| 0.37653($p$, $A$) | 2 ← 4 | 1.01301 | 1.408 | 5.409E-02 | 0.452E-03 |
| 0.41297($r$, $B$) | 2 ← 5 | 0.72915 | 1.013 | 5.135E-02 | 0.429E-03 |
| 0.44941($t$, $C$) | 2 ← 6 | 0.61942 | 0.861 | 5.622E-02 | 0.470E-03 |
| 0.46156($u$, $D$) | 2 ← 7 | 0.54544 | 0.758 | 5.363E-02 | 0.448E-03 |
| 0.47370 | 2 ← 9 | 0.20018 | 0.278 | 2.128E-02 | 0.178E-03 |
| 0.48585($v$) | 2 ← 11 | 0.39041 | 0.543 | 4.477E-02 | 0.374E-03 |
| 0.49799 | 2 ← 15 | 0.13502 | 0.188 | 1.668E-02 | 0.139E-03 |
| VIII. Route h($-2.90372 \leftarrow E_{\text{continuum}}$; only $E_{\text{continuum}}$ values are shown) | | | | | |
| 2.92723 | 0.02455 | 0.374E-03 | 0.520E-03 | 0.00938 | 0.784E-04 |
| 3.01226 | 0.10958 | 0.101E-03 | 0.140E-03 | 0.00275 | 0.230E-04 |
| 3.06084 | 0.15816 | 0.171E-03 | 0.238E-03 | 0.00491 | 0.410E-04 |
| 3.07299 | 0.17031 | 0.209E-03 | 0.291E-03 | 0.00607 | 0.507E-04 |
| 3.09728 | 0.19460 | 0.284E-03 | 0.395E-03 | 0.00845 | 0.706E-04 |
| 3.10943 | 0.20675 | 0.166E-03 | 0.230E-03 | 0.00498 | 0.416E-04 |
| 3.12157 | 0.21889 | 0.118E-03 | 0.164E-03 | 0.00358 | 0.299E-04 |
| 3.13372 | 0.23104 | 0.277E-03 | 0.385E-03 | 0.00851 | 0.712E-04 |
| 3.14587 | 0.24319 | 0.237E-03 | 0.330E-03 | 0.00738 | 0.617E-04 |
| 3.20660 | 0.30392 | 0.322E-03 | 0.448E-03 | 0.01063 | 0.888E-04 |
| 3.21874 | 0.31606 | 0.561E-03 | 0.779E-03 | 0.01870 | 0.156E-03 |
| 3.24304 | 0.34036 | 0.196E-03 | 0.273E-03 | 0.00670 | 0.560E-04 |
| 3.27947 | 0.37679 | 0.324E-03 | 0.450E-03 | 0.01142 | 0.955E-04 |
| 3.29162 | 0.38894 | 0.660E-03 | 0.917E-03 | 0.02353 | 0.197E-03 |
| 3.30377 | 0.40109 | 0.549E-03 | 0.763E-03 | 0.01981 | 0.166E-03 |
| 3.31591 | 0.41323 | 0.111E-03 | 0.155E-03 | 0.00406 | 0.339E-04 |
| 3.34020 | 0.43752 | 0.282E-03 | 0.392E-03 | 0.01051 | 0.878E-04 |
| 3.35235 | 0.44967 | 0.125E-03 | 0.173E-03 | 0.00469 | 0.392E-04 |
| 3.36450 | 0.46182 | 0.157E-03 | 0.219E-03 | 0.00560 | 0.510E-04 |
| 3.38879 | 0.48601 | 0.218E-03 | 0.303E-03 | 0.00849 | 0.709E-04 |
| 3.41308 | 0.51040 | 0.220E-03 | 0.305E-03 | 0.00874 | 0.730E-04 |
| 3.43737 | 0.53469 | 0.319E-03 | 0.444E-03 | 0.01297 | 0.108E-03 |
| 3.44952 | 0.54684 | 0.120E-03 | 0.166E-03 | 0.00491 | 0.410E-04 |
| 3.55884 | 0.65616 | 0.103E-03 | 0.143E-03 | 0.00463 | 0.387E-04 |
| 3.58312 | 0.68044 | 0.102E-03 | 0.142E-03 | 0.00470 | 0.393E-04 |

(Continued)

**TABLE I**
**(Continued)**

| $\omega$ (Label in Figs. 13 and 14) | Transitions | PSD($\omega$) | % Total PSD | RSD($\omega$) | % Total RSD |
|---|---|---|---|---|---|
| IX. Route i (He** $\leftarrow E_{continuum}$, SIT is the second-ionization threshold, i.e., zero-energy)[a] | | | | | |
| 0.13361 | $5p^2(^1D) \leftarrow$ SIT | 5.30107 | 7.368 | 1.264E-02 | 0.106E-03 |
| 0.14575 | $5s^2(^1S) \leftarrow$ SIT | 2.89206 | 4.020 | 0.896E-02 | 0.748E-04 |
| 0.17005 | $4s5s(^1S) \leftarrow$ SIT | 1.14417 | 1.590 | 0.563E-02 | 0.470E-04 |
| 0.19434 | $4s4p(^1P) \leftarrow$ SIT | 0.09152 | 0.127 | 0.672E-03 | 0.561E-05 |
| 0.20649 | $4s^2(^1S) \leftarrow$ SIT | 0.05136 | 0.0714 | 0.452E-03 | 0.378E-05 |
| 0.23078 | $37sp(+)(^1P) \leftarrow$ SIT | 0.38984 | 0.542 | 0.479E-02 | 0.400E-04 |
| 0.24292 | $35sp(+)(^1P) \leftarrow$ SIT | 0.02670 | 0.0371 | 0.383E-03 | 0.320E-05 |
| 0.26722 | $3d5d(^1G) \leftarrow$ SIT | 0.43206 | 0.600 | 0.00824 | 0.689E-04 |
| 0.27936 | $3s5s(^1S) \leftarrow$ SIT | 0.06820 | 0.0948 | 0.00149 | 0.124E-04 |
| 0.29151 | $3s4s(^1S) \leftarrow$ SIT | 0.34233 | 0.476 | 0.00848 | 0.709E-04 |
| 0.31580 | $3d^2(^1G) \leftarrow$ SIT | 0.12545 | 0.174 | 0.00395 | 0.330E-04 |
| 0.32795 | $3p^2(^1D) \leftarrow$ SIT | 0.01845 | 0.0256 | 0.651E-03 | 0.544E-05 |
| 0.35224 | $3s^2(^1S) \leftarrow$ SIT | 0.17902 | 0.249 | 0.00782 | 0.654E-04 |
| 0.51014 | $26sp(+)(^1P) \leftarrow$ SIT | 2.27390 | 3.160 | 0.30188 | 0.252E-02 |
| 0.52229 | $2s5s(^1S) \leftarrow$ SIT | 0.97000 | 1.348 | 0.13820 | 0.116E-02 |
| 0.53443 | $2p4p(^1D) \leftarrow$ SIT | 4.75865 | 6.614 | 0.72638 | 0.607E-02 |
| 0.54658 | $2s4s(^1S) \leftarrow$ SIT | 3.41787 | 4.750 | 0.55810 | 0.466E-02 |
| 0.57087 | $2p3p(^1P) \leftarrow$ SIT | 0.23010 | 0.320 | 0.04281 | 0.358E-03 |
| 0.59516 | $2s3s(^1S) \leftarrow$ SIT | 0.05256 | 0.073 | 0.01108 | 0.926E-04 |
| 0.69233 | $2s2p(^1P) \leftarrow$ SIT | 0.36263 | 0.504 | 0.12034 | 0.101E-02 |
| 0.70448 | $2p^2(^1D) \leftarrow$ SIT | 0.93265 | 1.296 | 0.32608 | 0.273E-02 |
| 0.77736 | $2s^2(^1S) \leftarrow$ SIT | 1.77318 | 2.464 | 0.83294 | 0.696E-02 |
| X. Route j (He* $\leftarrow E_{continuum}$)[b] | | | | | |
| 2.05271 | $1s3p(^1P) \leftarrow$ SIT | 0.530E-02 | 0.00736 | 0.04580 | 0.383E-03 |
| 2.06485 | $2s3s(^1S) \leftarrow$ SIT | 0.598E-03 | 0.831E-03 | 0.00526 | 0.440E-04 |
| 2.12559 | $1s2p(^1P) \leftarrow$ SIT | 0.643E-02 | 0.00893 | 0.06171 | 0.516E-03 |
| 2.14988 | $1s2s(^1S) \leftarrow$ SIT | 0.308E-03 | 0.428E-03 | 0.00306 | 0.256E-04 |
| XI. Route k | | | | | |
| Overlaps on the entire range from $\omega = 0.01214$ | | | | | |

Many other transitions occur with smaller PSD($\omega$). Transitions corresponding to a particular frequency overlap on one another (see Figs. 13 and 14). All quantities are in atomic units.

[a] Transitions also occur from continuum states above the SIT to the above He** states.

[b] Transitions also occur from continuum states above the SIT to the above He* states.

sufficiently late, keeping the laser field switched-on all through. Obviously, the complexion of the interacting system and the relative importance of various effects at that time would change in letting the system evolve to the asymptotic zero value of the laser field at infinite time. However, it is expected that even at this late time in our present study (not asymptotic) the system would manifest all the important physical effects which are responsible for the final experimental outcome. A limitation on computing resources have prevented our following the system's evolution up to the asymptotic time. However, in view of the fact that our principal objective was to study the mechanism of He–laser interaction this limitation is not significant, especially because our results are consistent with current experimental and other theoretical results. Such detailed contact between the hydrodynamical analogy to quantum mechanics and recent experimental information enables us to make predictions such as transitions in Table I and high harmonic generation in diatomic molecules [75] which need to be verified experimentally. It also indicates that the hydrodynamical analogy,

**TABLE II**
**High harmonic generation, $n\omega_L$, $3 \leqslant n(\text{odd}) \leqslant 21$, at $t = 517.29647$ au (12.512833 fs).**

| Frequency (closest $n$) | PSD | % Total PSD | RSD | % Total RSD |
|---|---|---|---|---|
| 0.4130(3) | 0.7291 | 1.0134 | 0.5135E-01 | 0.4292E-03 |
| 0.6923(5) | 0.3626 | 0.5040 | 0.1203 | 0.1006E-02 |
| 0.9717(7) | 0.6753E-01 | 0.09385 | 0.6195E-01 | 0.5178E-03 |
| 1.2389(9) | 0.2827 | 0.3929 | 0.5376 | 0.4493E-02 |
| 1.5183(11) | 0.1246E-02 | 0.1732E-02 | 0.4362E-02 | 0.3646E-04 |
| 1.7976(13) | 0.3346E-02 | 0.4650E-02 | 0.01944 | 0.1624E-03 |
| 2.0770(15) | 0.4928E-02 | 0.6849E-02 | 0.04415 | 0.3690E-03 |
| 2.3442(17) | 0.1279E-02 | 0.1778E-02 | 0.01648 | 0.1377E-03 |
| 2.6236(19) | 0.1970E-03 | 0.2738E-03 | 0.3558E-02 | 0.2974E-04 |
| 2.9029(21) | 0.2761E-03 | 0.3838E-03 | 0.6755E-02 | 0.5646E-04 |

which has never been viewed by ''mainstream quantum mechanics'' with much favor, needs to be taken seriously. It is particularly gratifying that the intuitive mechanistic routes a–k are all validated by the results to a considerable degree of accuracy. Such transparency and visualization are obvious benefits of a density-based approach.

**ACKNOWLEDGMENTS**

We thank the Department of Atomic Energy, Bombay, as well as the Council of Scientific and Industrial Research, New Delhi, for financial support. Thanks are also due to the Jawaharlal Nehru Centre for Advanced Scientific Research, Bangalore, for providing additional support.

## References

1. K. Burnett, V. C. Reed, and P. L. Knight, J. Phys. B: At. Mol. Opt. Phys. **26**, 561 (1993).
2. M. H. Mittleman, *Introduction to the Theory of Laser–Atom Interactions* (Plenum Press, New York, 1993).
3. M. Gavrilla, Ed., *Atoms in Intense Laser Fields* (Academic Press, Boston, 1992).
4. B. Piraux, Ed., in *Proceedings of the Workshop, Super Intense Laser Atom Physics (SILAP) III* (Plenum Press, New York, 1994).
5. K. C. Kulander, Phys. Rev. A **36**, 2726 (1987).
6. J. Javanainen, J. H. Eberly, and Q. Su, Phys. Rev. A **38**, 3430 (1988).
7. J. N. Bardsley, A. Szöke, and M. J. Comella, J. Phys. B: At. Mol. Opt. Phys. **21**, 3899 (1988).
8. J. H. Eberly, Q. Su, and J. Javanainen, Phys. Rev. Lett. **62**, 881 (1989).
9. K. C. Kulander and B. W. Shore, Phys. Rev. Lett. **62**, 524 (1989).
10. K. C. Kulander, Ed., *Time-Dependent Methods for Quantum Dynamics: A Thematic Issue of Computer Physics Communications* (North-Holland, Amsterdam, 1991).
11. J. L. Krause, K. J. Schaefer, and K. C. Kulander, Phys. Rev. Lett. **68**, 3535 (1992).
12. S. Chelkowski, T. Zuo, and A. D. Bandrauk, Phys. Rev. A **46**, R 5342 (1992).
13. V. C. Reed and K. Burnett, Phys. Rev. A **46**, 424 (1992).
14. A. L'Huillier, Ph. Balcou, S. Candel, K. J. Schafer, and K. C. Kulander, Phys. Rev. A **46**, 2778 (1992).
15. M. Lewenstein, Ph. Balcou, M. Yu. Ivanov, A. L'Huillier, and P. B. Corkum, Phys. Rev. A **49**, 2117 (1994).
16. R. M. Potvleige and R. Shakeshaft, Phys. Rev. A **40**, 3061 (1989).
17. P. B. Corkum, N. H. Burnett, and F. Brunel, Phys. Rev. Lett. **62**, 1259 (1989).
18. S. Augst, D. Strickland, D. D. Meyerhofer, S. L. Chin, and J. H. Eberly, Phys. Rev. Lett. **63**, 2212 (1989).
19. G. G. Paulus, W. Nicklich, H. Xu., P. Lambropoulos, and H. Walther, Phys. Rev. Lett. **72**, 2851 (1994).
20. K. J. Schafer, B. Yang, L. F. Dimauro, and K. C. Kulander, Phys. Rev. Lett. **70**, 1599 (1993).
21. J. Peatross, B. Buerke, and D. D. Meyerhofer, Phys. Rev. A **47**, 1517 (1993).
22. E. Mevel, P. Breger, R. Trainham, G. Petite, P. Agostini, A. Migus, J. P. Chambaret, and A. Antonetti, Phys. Rev. Lett. **70**, 406 (1993).
23. D. N. Fittinghoff, P. R. Bolton, B. Chang, and K. C. Kulander, Phys. Rev. Lett. **69**, 2642 (1992).
24. P. B. Corkum, Phys. Rev. Lett. **71**, 1994 (1993).
25. J. H. Eberly and K. C. Kulander, Science **262**, 1229 (1993).
26. A. Sanpera, Phys. Rev. A **49**, 1967 (1994).
27. K. C. Kulander, K. J. Schafer, and J. L. Krause, in *Proceedings of the Workshop, Super Intense Laser Atom Physics* (*SILAP*) *III* (Plenum Press, New York, 1994).
28. W. Becker, S. Long, and J. K. McIver, Phys. Rev. A **41**, 4112 (1990).
29. L. V. Keldysh, Zh. Eksp. Teor. Fiz. **47**, 1945 (1964); *Idem.*, Sov. Phys. JETP **20**, 1307 (1965).

30. M. Pont, N. R. Walet, M. Gavrila, and C. W. McCurdy, Phys. Rev. Lett. **61**, 939 (1988).
31. X. Tang, H. Rudolph, and P. Lambropoulos, Phys. Rev. Lett. **65**, 3269 (1990).
32. H. R. Reiss, J. Phys. B: At. Mol. Phys. **20**, L79 (1987).
33. R. V. Jensen and B. Sundaram, Phys. Rev. Lett. **65**, 1964 (1990).
34. B. M. Deb and P. K. Chattaraj, Phys. Rev. A **39**, 1696 (1989).
35. B. M. Deb, P. K. Chattaraj, and S. Mishra, Phys. Rev. A **43**, 1248 (1991); P. K. Chattaraj, Int. J. Quantum Chem. **41**, 845 (1992).
36. R. W. Heather, Comput. Phys. Commun. **63**, 446 (1991).
37. A. S. Bamzai and B. M. Deb, Rev. Mod. Phys. **53**, 95, 593 (1981).
38. S. K. Ghosh and B. M. Deb, Phys. Rep. **92**, 1 (1982).
39. B. M. Deb and S. K. Ghosh, J. Chem. Phys. **77**, 342 (1982).
40. S. K. Ghosh and B. M. Deb, Int. J. Quantum Chem. **22**, 871 (1982).
41. B. M. Deb and S. K. Ghosh, in *The Single-particle Density in Physics and Chemistry*, N. H. March and B. M. Deb, Eds. (Academic Press, London, 1987).
42. B. M. Deb and P. K. Chattatraj, in *Solitons: Introduction and Applications*, M. Lakshmanan, Ed. (Springer-Verlag, Berlin, 1988).
43. L. J. Bartolotti, Phys. Rev. A **24**, 1661 (1981).
44. E. Runge and E. K. U. Gross, Phys. Rev. Lett. **52**, 997 (1984).
45. E. K. U. Gross and W. Kohn, in *Density Functional Theory of Many-Electron Systems*, S. B. Trickey, Ed. (Academic Press, New York, 1991).
46. R. G. Parr and W. Yang, *Density-Functional Theory of Atoms and Molecules* (Oxford University Press, New York, 1989).
47. E. S. Kryachko and E. V. Ludena, *Energy Density Functional Theory of Many-Electron Systems* (Kluwer, Dordrecht, 1990).
48. B. M. Deb and P. K. Chattaraj, Phys. Rev. A **45**, 1412 (1992).
49. B. M. Deb and S. K. Ghosh, Int. J. Quantum Chem. **23**, 1 (1983).
50. A. Giusti-Suzor, X. He, O. Atabek, and F. H. Mies, Phys. Rev. Lett. **64**, 515 (1990).
51. H. Tal-Ezer and R. Kosloff, J. Chem. Phys. **81**, 9 (1984).
52. Y. Sun, D. J. Kouri, D. W. Schwenke, and D. G. Truhlar, Comp. Phys. Commun. **63**, 51 (1991).
53. B. Kr. Dey and B. M. Deb, to be published.
54. J. L. Richardson, Comp. Phys. Commun. **63**, 84 (1991).
55. A. R. Mitchell, *Computational Methods in Partial Differential Equations* (Wiley, London, 1976), Chaps. 2 and 3.
56. E. Clementi and C. Roetti, At. Data Nucl. Data. Tables **14**, 174 (1974).
57. G. D. Smith, *Numerical Solution of Partial Differential Equations* (Oxford University Press, London, 1965).
58. P. M. Morse and H. Feshbach, *Methods of Theoretical Physics*, (McGraw-Hill, New York, 1953), Part II, p. 1263.
59. K. C. Kulander, K. R. Sandhya Devi, and S. E. Koonin, Phys. Rev. A **25**, 2968 (1982).
60. K. R. Sandhya Devi and J. D. Garcia, Phys. Rev. A **30**, 600 (1984).
61. E. Bohl, in *Stability in the Numerical Solution of Nonlinear Problems*, T. H. Baker and C. Phillips, Eds. (Clarendon Press, Oxford, 1981), pp. 171–183.
62. H. De Readt, Comput. Phys. Rep. **7**, 1 (1987).
63. M. D. Feit and J. A. Fleck, Jr., J. Chem. Phys. **80**, 2578 (1984).
64. B. Kr. Dey and B. M. Deb, Int. J. Quantum Chem. **56**, 707 (1995).
65. B. Kr. Dey and B. M. Deb, Pramana—J. Phys. **48**, L849 (1997).
66. D. J. Nagel, P. G. Burkhalter, C. M. Dozier, J. F. Holzrichter, B. M. Klein, J. M. McMahon, J. A. Stamper, and R. R. Witlock, Phys. Rev. Lett. **33**, 743 (1974).
67. F. C. Young, Phys. Rev. Lett. **33**, 747 (1974).
68. A. J. Thakkar and V. H. Smith, Jr., Phys. Rev. A **15**, 1 (1997).
69. C. A. Ullrich, U. J. Gossmann, and E. K. U. Gross, Phys. Rev. Lett. **74**, 872 (1995).
70. C. A. Ullrich, U. J. Gossmann, and E. K. U. Gross, Ber. Bunsenges. Phys. Chem. **99**, 488 (1995).
71. E. K. U. Gross, J. F. Dobson, and M. Petersilka, in *Density Functional Theory*, R. F. Nalewajski, Ed., Springer Series Topics in Current Chemistry (Springer, Berlin, 1996).
72. C. A. Ullrich, S. Erhard, and E. K. U. Gross, in *Super Intense Laser Atom Physics IV*, H. G. Muller, Ed. (Kluwer, Dordrecht, 1996).
73. C. A. Ullrich and E. K. U. Gross, Comments At Mol. Phys. **33**, 211 (1997).
74. E. Engel and S. H. Vosko, Phys. Rev. A **47**, 2800 (1993).
75. J. B. Krieger, Y. Li, and G. J. Iafrate, in *Density Functional Theory*, E. K. U. Gross and R. M. Dreizler, Eds., NATO ASI Series (Plenum Press, New York, 1994).
76. B. Kr. Dey and B. M. Deb, Chem. Phys. Lett. **276**, 157 (1997).